ARTICLE IN PRESS

Communications Materials

https://doi.org/10.1038/s43246-026-01120-1

Article in Press

Morphotaxial Cu doping in monolayer MoS_2 for high-performance optoelectronics

Received: 19 September 2025

Accepted: 19 February 2026

Cite this article as: Rajput, M., Shukla, A., Mahapatra, A. *et al.* Morphotaxial Cu doping in monolayer MoS_2 for high-performance optoelectronics. *Commun Mater* (2026). https://doi.org/10.1038/s43246-026-01120-1

Manisha Rajput, Ashutosh Shukla, Avinash Mahapatra, Swapneswar Bisoi, G. V. Pavan Kumar & Atikur Rahman

We are providing an unedited version of this manuscript to give early access to its findings. Before final publication, the manuscript will undergo further editing. Please note there may be errors present which affect the content, and all legal disclaimers apply.

If this paper is publishing under a Transparent Peer Review model then Peer Review reports will publish with the final article.

ARTICLE IN PRESS

© The Author(s) 2026. **Open Access** This article is licensed under a Creative Commons Attribution-NonCommercial-NoDerivatives 4.0 International License, which permits any non-commercial use, sharing, distribution and reproduction in any medium or format, as long as you give appropriate credit to the original author(s) and the source, provide a link to the Creative Commons licence, and indicate if you modified the licensed material. You do not have permission under this licence to share adapted material derived from this article or parts of it. The images or other third party material in this article are included in the article's Creative Commons licence, unless indicated otherwise in a credit line to the material. If material is not included in the article's Creative Commons licence and your intended use is not permitted by statutory regulation or exceeds the permitted use, you will need to obtain permission directly from the copyright holder. To view a copy of this licence, visit http://creativecommons.org/licenses/by-nc-nd/4.0/.

ARTICLE IN PRESS

Morphotaxial Cu doping in Monolayer MoS_2 for High-performance Optoelectronics

Manisha Rajput,* Ashutosh Shukla, Avinash Mahapatra, Swapneswar Bisoi, G V Pavan Kumar, and Atikur Rahman*

Department of Physics and IHUB Quantum Technology Foundation, Indian Institute of Science Education and Research, Pune-411008, India

E-mail: manisha@students.iiserpune.ac.in; atikur@iiserpune.ac.in

ARTICLE IN PRESS

Abstract

Doping is crucial for semiconductor technology, enabling the design of integrated circuits, microprocessors, and other advanced optoelectronic devices with desired properties. The emergence of two-dimensional (2D) materials has opened pathways for atomic-scale integration. However, their 2D nature limits conventional ion implantation methods for doping, which poses a significant barrier to further device development and optimization. Here, we report a solvent-based cation-exchange morphotaxy that enables substitutional incorporation of Cu atoms into CVD-grown MoS_2 monolayers. This approach induces stable p-type doping, suppressing dark current by four orders of magnitude and enhancing the light-to-dark current ratio by over 1,000-fold compared to pristine MoS_2. The substitutional Cu incorporation modifies the trap-state landscape, leading to faster photoresponse and reduced noise. As a result, Cu-doped MoS_2 photodetectors achieve specific detectivity values up to 10^{14} Jones and response times improved by more than an order of magnitude, outperforming many previously reported doped transition metal dichalcogenide devices. This scalable and CMOS-compatible

ARTICLE IN PRESS

doping strategy provides a pathway for defect and electronic structure engineering in 2D semiconductors, opening new opportunities for high-performance optoelectronics, including neuromorphic and spintronic applications.

Introduction

Two-dimensional (2D) materials have emerged as a versatile platform for exploring novel optical, electronic, and optoelectronic phenomena due to their atomic thickness, tunable band structure, and high surface-to-volume ratio. Following the success of graphene, transition metal dichalcogenides (TMDs) have attracted significant attention. Among them, molybdenum disulfide (MoS_2) is one of the most widely investigated materials. Monolayer MoS_2 is a direct gap semiconductor with a bangap of 1.8 eV,[1,2] making it suitable for digital electronics as well as optoelectronic applications such as light-emitting devices,[3,4] photodetectors,[5–7] and solar cells.[8]

A major challenge in MoS_2-based photodetectors is high dark current and persistent photoconductance (PPC), which originates from the trapping of minority carriers by surface-bound water molecules, other adsorbates, and intrinsic defects in MoS_2 and the underlying dielectric.[9–12] Although carrier trapping enhances photoconductive gain by extending carrier lifetime, it severely degrades the response speed, as PPC can persist from minutes to hours.[12–15]

Various strategies, including surface passivation and field-effect modulation, have been explored to suppress PPC by reducing trap density or controlling trap occupancy.[11] However, these approaches often compromise device sensitivity by weakening trap-assisted gain mechanisms.[9] Another strategy involves photoconductive detectors based on vertical carrier separation and interfacial trapping, such as vertically stacked van der Waals (vdW) heterostructures[16] and surface-coupled quantum dot.[17,18] In these devices, fast photoconductive gain arises from fast charge transfer at the interface, driven by the built-in electric field and type-II band alignment. However, vdW heterojunctions fabricated via mechanical ex-

ARTICLE IN PRESS

foliation face significant challenges in large-area integration and scalability, while quantum dot-integrated devices often suffer from surface trap states and long-term stability issues.

Doping is a promising method to tailor the optoelectronic properties of 2D materials by changing carrier density, trap dynamics, and the Fermi level.[19–23] Current approaches for the doping of these layered materials mainly focus on electrostatic gating, surface functionalization, or charge-transfer doping.[24–30] However, the practical implementation of these strategies is often limited by electrical breakdown and molecular instability. Moreover, the substitution of host atoms with dopants, as widely used in conventional semiconductors where the doping is secured and stabilized by covalent bonding inside the lattice, has gained significant attention for its potential to develop high-performance electronics and optoelectronics devices.[20,21,31–41]

While ion implantation is a cornerstone of silicon technology, it is incompatible with 2D materials; cation exchange via morphotaxy provides a promising alternative for substitutional doping of 2D materials. Lam et al. coined the term "morphotaxy" from the Greek prefix "morpho-" (shape), referring to a synthesis approach that uses an existing 2D material as a template, producing a product with the same shape as the parent crystal.[42] This approach takes advantage of already existing 2D material as a template to initiate the reaction, resulting in the product having the same shape as the parent crystal.[42,43] Morphotaxy can enable non-vdW heterostructures, vdW heterostructures, passivation of ambient reactive 2D materials, or doping of 2D materials.[42] Oxidation based morphotaxy has been employed to dope or modulate the properties of 2D materials for better photodetector and artificial synaptic devices.[44,45] Similarly, anionic-based morphotaxy provides a viable route to modify the electronic and optoelectronic behavior of devices constructed from 2D materials.[46,47]

In this work, we achieve substitutional Cu doping in MoS_2 monolayers through cation-exchange morphotaxy to tailor their optoelectronic properties, resulting in markedly improved photodetector performance. Cu-doping in MoS_2 monolayer was confirmed by Raman spectroscopy, photoluminescence (PL), X-ray photoelectron spectroscopy (XPS), high-resolution transmission electron microscopy (HRTEM), and energy-dispersive X-ray spectroscopy (EDS)

ARTICLE IN PRESS

ARTICLE IN PRESS

elemental mapping. A comprehensive statistical analysis was conducted on 70 devices, all fabricated with identical geometry (channel length: 4 μm, width: 10 μm), before and after doping. Prior to doping, most devices exhibited dark currents in the range of 1-10 nA, whereas after doping, the dark current was markedly suppressed to the 0.1-10 pA range. The $I_{\text{light}}/I_{\text{dark}}$ ratio of pristine MoS_2 devices predominantly lies between 10^1 and 10^2, while Cu-doped MoS_2 devices show a pronounced improvement, with ratios reaching approximately 10^4. In addition, the Cu-doped devices exhibit more than one order faster photoresponse compared to pristine MoS_2. The detectivity of pristine devices mostly falls within the range of 10^{11}-10^{12} Jones, whereas Cu-doped devices achieve values as high as 10^{12}-10^{14} Jones. These findings highlight a simple, scalable, and cost-effective doping strategy for CVD-grown MoS_2, offering a viable pathway toward the realization of high-performance optoelectronic devices.

ARTICLE IN PRESS

Results and discussion

Synthesis and Structural Characterization

Figure 1a shows the schematic of the cation-exchange morphotaxy for Cu doping in MoS_2 monolayer. First, monolayer MoS_2 flakes were grown on a Si/SiO_2(300 nm) substrate using the CVD technique (see the Experimental Section for details.). Then, we employed a solvent-based method to introduce the Cu doping into MoS_2 monolayer. Tetrakis(acetonitrile) copper(I) hexafluorophosphate was used as a precursor, and acetone was used as a solvent. Monovalent copper is disproportionate in solution according to the equation 1 .[48,49]

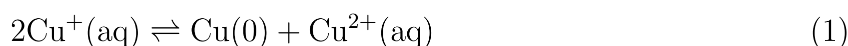

$$2\mathrm{Cu}^{+}(\mathrm{aq}) \rightleftharpoons \mathrm{Cu}(0) + \mathrm{Cu}^{2+}(\mathrm{aq}) \tag{1}$$

As shown in Figure 1a CVD-grown MoS_2 on Si/SiO_2 was immersed in a solution of 10 ml acetone and 10 mg of precursor for 30 minutes at 50 °C. After the reaction, the substrate was rinsed with hot acetone and isopropyl alcohol (IPA) several times to remove the residues and

ARTICLE IN PRESS

then dried in N_2 flow. Figure 1b and 1c show the optical images of CVD-grown monolayer MoS_2 before and after the reaction, respectively. After the reaction, the flake retains its original shape and dimensions, a key advantage of morphotaxy[43] with no residue left on the sample surface. Figure 1d presents the Raman spectra of pristine and Cu-doped MoS_2. Raman spectra of pristine MoS_2 exhibit two peaks, an in-plane vibration mode E^1_{2g} at ∼383.76 cm^{-1} and an out-of-plane vibration mode A_{1g} at ∼401.88 cm^{-1}. The difference between the A_{1g} and E^1_{2g} peak positions was found to be ∼18.12 cm^{-1}, which indicated that the synthesized MoS_2 is monolayer.[50] After the reaction, we see a blue shift and reduced full width at half maxima (FWHM) of A_{1g} peak. By studying the in-situ Raman spectra of top-gated monolayer MoS_2 FETs, it has been observed that the A_{1g} mode softens and broadens, whereas the E^1_{2g} mode remains largely unaffected upon electron doping.[51] These experimental findings were supported by first-principles density functional theory calculations and a group-theoretical analysis of symmetry. The electron-phonon coupling (EPC) was calculated for both the A_{1g} and $E^1{}_{2g}$ modes. The A_{1g} phonon mode corresponds to the out-of-plane vibration of sulfur atoms, moving in opposite directions along the *c*-axis (perpendicular to the basal plane), whereas the $E^1{}_{2g}$ mode involves in-plane vibrations of both molybdenum and sulfur atoms in the basal plane. The A_{1g} mode exhibits the symmetry of the lattice, so structural distortions in this mode do not break the symmetry of MoS_2. As a result, the A_{1g} mode shows strong EPC, making it more sensitive to electron doping, while the coupling of the $E^1{}_{2g}$ mode with electrons is only weakly dependent on doping. Electron doping fills anti-bonding states in the conduction band, weakening the bonds and softening the A_{1g} mode. Since the phonon linewidth is proportional to the EPC associated with a particular mode, the increase in the linewidth of the A_{1g} mode reflects the strengthening of EPC with doping. Conversely, in our observations, the A_{1g} peak frequency increases, and its FWHM decreases, suggesting a reduction in electron concentration or the introduction of p-type doping after the reaction. Previous theoretical studies have reported that Cu substitution in MoS_2 leads to p-type doping.[52,53] Notably, the E^1_{2g} peak position and its FWHM remain largely

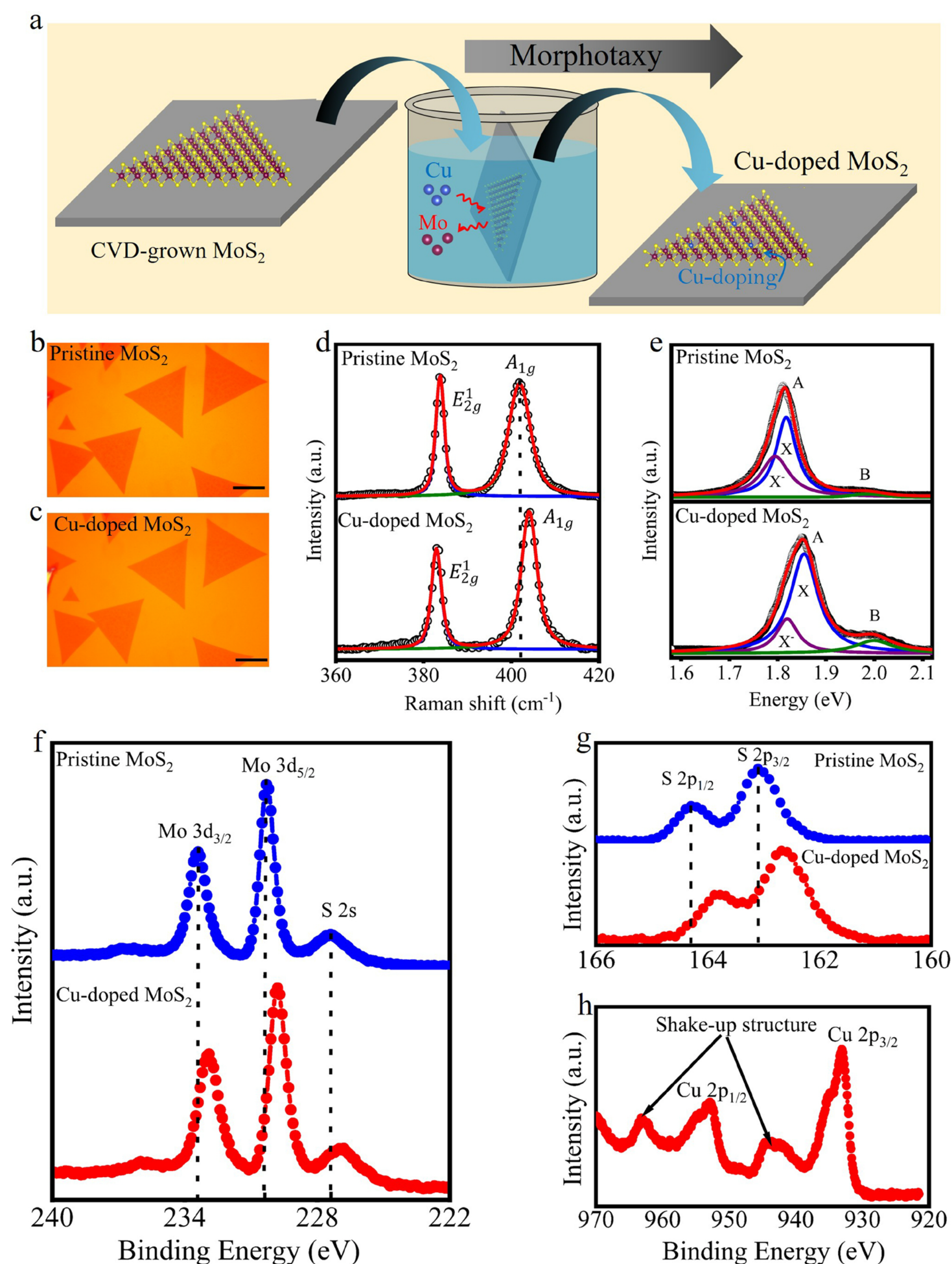

Figure 1: **Structural characterization of MoS_2 before and after Cu doping.** (a) schematic of cationic-exchange morphotaxy (b) Optical image of CVD-grown MoS_2 (scale bar 20 μm). (c) Optical image of CVD-grown MoS_2 (scale bar 20 μm) after Cu doping (d) Raman spectra before and after doping (e) PL spectra before and after doping (f) XPS of Mo 3d core spectra before and after doping (g) XPS of S 2s before and after doping. (h) XPS of Cu 2p spectra of Cu doped MoS_2.

ARTICLE IN PRESS

unchanged. Figure 1e shows the fitted PL spectra of pristine and doped MoS_2. The PL spectra reveal one prominent peak corresponding to the A-exciton and another less prominent peak corresponding to the B-exciton. The A exciton peak can be deconvoluted into two components, attributed to the negatively charged trion (X^-) and the neutral exciton (X) peak. PL spectra clearly show that in pristine MoS_2, the PL spectral weight of the negative trion (X^-) peak is greater than that of the exciton (X) peak. This observation aligns with previously reported results, where trion (X^-) recombination is dominant in as-prepared monolayer MoS_2 due to unintentional high electron (n-type) doping.[54] In Cu-doped MoS_2, PL spectra are dominated by the exciton peak, and the overall spectra are blue-shifted. These findings are consistent with the literature reports for p-type MoS_2, where the reduction in negative carriers results in fewer trion formation.[55–57] Similar results have been observed previously in gate-dependent PL spectra of MoS_2, where at positive gate voltages (p-type doping), exciton peak becomes dominant, and at negative gate voltages (n-type doping), trion peak becomes dominant.[54] Our results from Raman and PL measurement strongly suggest a decrease in the number of negative charge carriers after the reaction. Further, we performed XPS measurements on the pristine and Cu-doped MoS_2 to confirm the doping. Figures 1f and 1g present the Mo 3d and S 2p core spectra before and after doping. After doping, all peaks shift to lower binding energy by $\sim$ 0.5 eV. Specifically, Mo $3d_{3/2}$ shifts from 233.4 to 232.9 eV, Mo $3d_{5/2}$ shifts from 230.3 to 229.8 eV, S $2p_{1/2}$ shifts from 164.3 to 163.8 eV, and S $2p_{3/2}$ shifts from 163.1 to 162.6 eV. Binding energy shifts in XPS spectra for core-level electrons have been previously utilized to identify the doping type in MoS_2.[58,59] After the reaction, the Mo and S XPS peaks shift to lower binding energies, indicating a shift in the Fermi level toward the valence band maximum and reflecting p-type doping in the MoS_2.[55,60] Figure 1h shows the Cu 2p XPS spectra displaying Cu $2p_{3/2}$ at $\sim$ 933 eV and Cu $2p_{1/2}$ at $\sim$ 953 eV, indicating that Cu is chemically reacting with MoS_2. Additionally, Cu 2p spectra exhibit strong satellite peaks $\sim$ 963 eV and $\sim$ 943 eV. These strong satellite shake-up features and peak positions of Cu $2p_{3/2}$ and Cu $2p_{1/2}$ confirm that Cu is present in the +2 state.[61–63] The

ARTICLE IN PRESS

XPS results strongly suggest that copper is replacing molybdenum through cation exchange. Previous theoretical reports have shown that the formation energies for substituting Mo with Cu in MoS_2 are non-positive, suggesting that substitutional doping of Cu atoms is feasible in MoS_2 matrices.[52,53] The doping concentration, as determined from the XPS data, was estimated to be approximately 5%.[38,64] Such copper-based cation exchange has been observed in other materials, such as Bi_2Se_3 and SnS_2.[65,66] It has been observed that layered, 2D SnS_2 can be transformed to nonlayered Cu_2SnS_3 via cation exchange.[66] The synthesis of vertical Cu_2S–CdS heterostructures,[67] and formation of Cu_xSe from CdSe through copper cation exchange in solution have also been reported.[68]

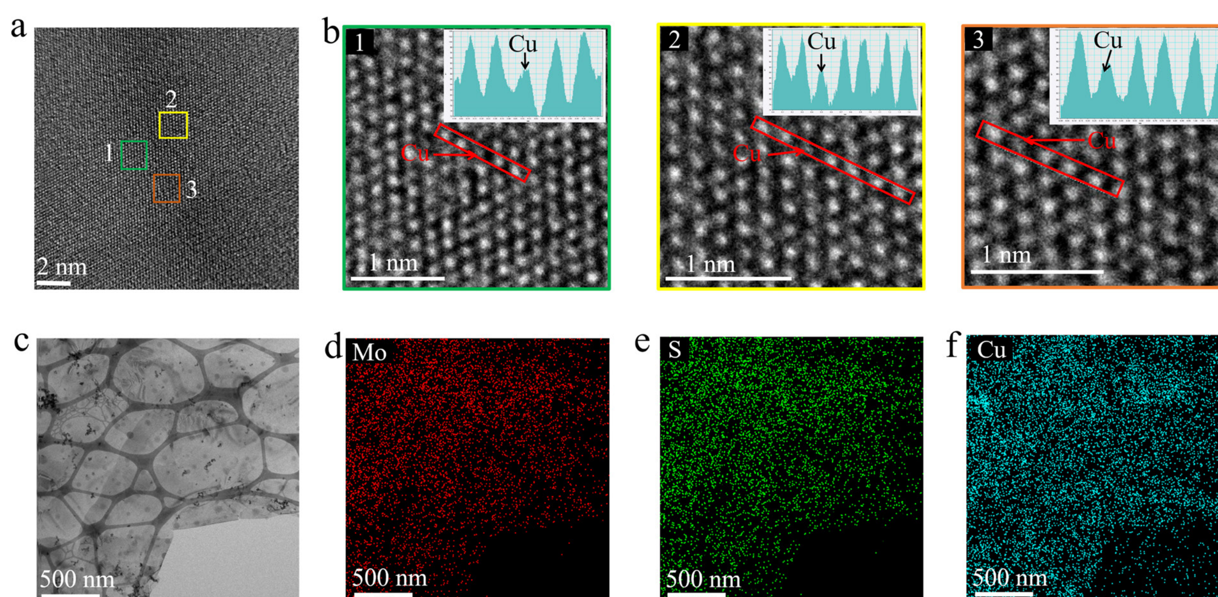

Figure 2: **HRTEM image and EDX elemental map of doped MoS_2.** (a) HRTEM image of doped MoS_2. (b) Enlarged images of selected rectangle areas, shown in image a, 1 enlarged image of green rectangle, 2 enlarged image of yellow rectangle, 3 enlarged image of orange rectangle. Inset images show the intensity along the selected area in red. (c) Low magnification TEM image of doped MoS_2. (d) Corresponding EDX elemental map of Mo (e) EDX elemental map of S (f) EDX elemental map of Cu.

To gain deeper insight into the atomic structure of Cu-doped MoS_2, we employed HRTEM and EDX elemental mapping. **Figure** 2a presents the HRTEM image of doped MoS_2, while Figure 2b shows an enlarged view of three selected areas marked in Figure 2a (1 for the green rectangle, 2 for the yellow rectangle, and 3 for the orange rectangle). The intensity maps, shown in the inset of Figure 2b, were obtained from specific regions marked in red within

ARTICLE IN PRESS

Figure 2b. Compared to Mo (Z = 42), Cu (Z = 29) has an atomic number approximately 30% lower, which suggests that Cu atoms will produce a lower relative intensity. This is evident in Figure 2b, where the Cu atoms, indicated by red arrows, appear slightly darker compared to the Mo atoms. The intensity maps inset in Figure 2b clearly reveal that the Cu atoms exhibit lower intensity. The HRTEM images confirm that Cu is substituting at Mo sites, as indicated by the red arrows in Figure 2b. Figure 2c displays a low-magnification TEM image of Cu-doped MoS_2, while Figures 2d, 2e and 2f show the corresponding EDX elemental mappings for Mo, S, and Cu, respectively. From the mapping data, it is evident that the Cu is homogeneously distributed throughout the sample. These findings established the substitution of Mo with Cu atoms via cation exchange. To further elucidate the effect of Cu doping, the surface potential of pristine MoS_2 and Cu-doped MoS_2 was investigated using Kelvin probe force microscopy (KPFM) as shown in Figure S2. The average surface potential decreases significantly from ~330 mV for pristine MoS_2 to ~160 mV after Cu doping. Such a decrease in surface potential corresponds to an increase in the work function of MoS_2, as reported previously.[69] The increased work function indicates a downward shift of the Fermi level toward the valence band, providing clear evidence of p-type doping induced by Cu incorporation. Moreover, theoretical studies have reported that substituting Mo with Cu induces p-type doping.[52,53] Our experimental results from Raman, PL, KPFM and XPS also indicate p-type doping.

Optoelectronic properties

We have explored the optoelectronic properties of Cu-doped MoS_2 to understand the effect of cation exchange-based doping. Source/drain electrodes were fabricated using photolithography, followed by thermal vapour deposition of Cr/Au and a lift-off process. The heavily doped Si substrate was employed as the back gate electrode and 300 nm SiO_2 as gate dielectric. The optical image of the fabricated device is presented in Figure S3 with channel length 4 μm and width 10 μm. **Figure** 3a presents the output characteristics of a pristine MoS_2-based

ARTICLE IN PRESS

ARTICLE IN PRESS

device, i.e., the source-to-drain current (I_{DS}) as a function of source-to-drain voltage (V_{DS}) for various back gate voltages (V_{GS}). The observed approximate linear relationship between I_{DS} and V_{DS} indicates that the contacts are nearly Ohmic. Figure 3b shows the output characteristics of the Cu-doped MoS_2-based device. After Cu doping, a noticeable reduction in current is observed compared to the pristine device. Figures 3c and 3d present the transfer characteristics of pristine and Cu-doped MoS_2, respectively. These plots illustrate I_{DS} as a function of V_{GS} at a V_{DS} of 0.5 V, presented in both linear and logarithmic scales. The transfer characteristics of pristine MoS_2 exhibit n-type behaviour, as commonly reported in previous studies.[2]

ARTICLE IN PRESS

ARTICLE IN PRESS

Review figure 2.jpg

ARTICLE IN PRESS

Figure 3: **Electrical characterization of pristine and Cu-doped MoS_2.** (a) Output-characteristics of pristine MoS_2, I_{DS} versus V_{DS} for various gate voltage (V_{GS}). (b) Output-characteristics of Cu-doped MoS_2, I_{DS} versus V_{DS} for various gate voltage (V_{GS}) (c) Transfer-characteristics of pristine MoS_2, I_{DS} versus V_{GS} at V_{DS} = 0.5 V, left side (blue colour) in linear scale and right side (red colour) in logarithmic scale. (d) Transfer characteristics of Cu-doped MoS_2, I_{DS} versus V_{GS} at V_{DS} = 0.5 V, left side (blue colour) in linear scale and right side (red colour) in logarithmic scale. (e) Hysteresis in transfer-characteristics, for pristine MoS_2 in red colour, and for Cu-doped MoS_2 in blue colour, the arrow is showing the sweeping direction, V_{DS} was kept 0.5 V (f) Comparison of I_{DS} versus V_{DS} of pristine MoS_2 and Cu-doped MoS_2.

The field-effect mobility (μ_{FE}) was extracted from the peak transconductance using a parallel-plate gate capacitance model, and the threshold voltage (V_{TH}) was determined using

ARTICLE IN PRESS

the linear extrapolation method. It should be mentioned here that while calculating the mobility values we have not included the effect of contact resistance. From the transfer characteristics of pristine MoS_2, the extracted μ_{FE} and V_{TH} are approximately 11 $cm^2V^{-1}s^{-1}$ and -8 V, respectively. The on/off current ratio (I_{max}/I_{min}) is $\sim 10^6$, where I_{max} and I_{min} are the maximum and minimum drain currents obtained from the transfer characteristics at $V_{DS} = 0.5$ V. The subthreshold swing (SS), extracted over two order of magnitude change in drain current, is found to be 5.6 V/decade, and the peak transconductance is 6.3×10^{-3} μS/μm at $V_{DS} = 0.5$ V. Following Cu doping, the drain current in MoS_2 decreases markedly, accompanied by a positive shift in the threshold voltage to approximately 20 V, indicating suppression of the intrinsic n-type behavior. The field-effect mobility of the Cu-doped MoS_2 is reduced to ~ 4 $cm^2V^{-1}s^{-1}$. The on/off current ratio (I_{max}/I_{min}), obtained from the transfer characteristics, decreases to $\sim 10^3$, while the SS, extracted over two order of magnitude change in drain current, increases to 11.5 V/decade and the peak transconductance value 8.27×10^{-5} μS/μm. The p-branch observed in the transfer characteristics after Cu doping may arise from either p-type doping of the MoS_2 channel or Schottky barrier modulation at the contacts. However, KPFM and XPS analyses reveal a downward shift of the Fermi level of MoS_2 after Cu doping, indicating that the p-branch is governed by p-type channel doping rather than contact barrier modulation.

To contextualize our device performance, Table 1 presents a comparison of pristine MoS_2 n-FET and Cu-doped MoS_2 devices alongside recently reported high-performance MoS_2 and WSe_2 benchmarks from the literature. Key metrics, including on-state current (I_{ON}), SS, and V_{TH}, with the corresponding drain voltage (V_{DS}) and channel length (L_{ch}). As shown in Table1, the performance of the present devices is lower than that reported in these benchmark studies. This is primarily due to the relatively thick back-gate SiO_2 dielectric (300 nm), the larger channel lengths and CVD-grown MoS_2. Device performance can be further improved through contact engineering, integration of high-κ gate dielectrics, and channel-length scaling.

ARTICLE IN PRESS

ARTICLE IN PRESS

Table 1: **Comparison of pristine MoS_2 n-FETs and Cu-doped MoS_2 p-branch with representative high-performance n-type and p-type FETs.**

ccccccccc

Ref	Growth / Material / Type	Dielectric	L_{ch} (nm)	V_{DS} (V)	I_{ON} (μA/μm)	SS (mV
[40]	MOCVD MoS_2 (n-FET)	10 nm HfO_2	100	1	336	83
[70]	MOCVD WSe_2 (n-FET)	9 nm Al_2O_3/3 nm HfO_2/3 nm Al_2O_3	300	1	26	14
[71]	MOCVD MoS_2 (n-FET)	9 nm Al_2O_3/3 nm HfO_2/3 nm Al_2O_3	300	1	33	79
This work	Pristine MoS_2 (n-FET)	300 nm SiO_2	4000	0.5	0.18	560
[40]	MOCVD WSe_2 (p-FET)	10 nm HfO_2	100	1	306	74
[70]	MOCVD WSe_2 (p-FET)	9 nm Al_2O_3/3 nm HfO_2/3 nm Al_2O_3	300	1	16	24

ARTICLE IN PRESS

ARTICLE IN PRESS

cccccccccc

Ref	Growth / Material / Type	Dielectric	L_{ch} (nm)	V_{DS} (V)	I_{ON} (μA/μm)	SS (mV
[71]	MOCVD WSe_2 (p-FET)	9 nm Al_2O_3/3 nm HfO_2/3 nm Al_2O_3	300	1	10	45
[20]	MOCVD WSe_2 (p-FET)	10 nm HfO_2	100	-1	280	35
[21]	CVT $MoSe_2$ (p-FET)	25 nm Al_2O_3	50	1	212	30(
[72]	MOCVD WSe_2 (p-FET)	25 nm Al_2O_3	20	1	16	77
This work	Cu-doped MoS_2 (p-branch)	300 nm SiO_2	4000	0.5	2×10^{-5}	–-

ARTICLE IN PRESS

Figure 3e displays the hysteresis in the transfer characteristics, clearly showing that after Cu-doping, the threshold voltage has shifted to the positive side, compared to the pristine MoS_2. Several factors have been identified as potential causes for the observed hysteresis in the transfer characteristics, including electron trapping and de-trapping by adsorbed molecules on the MoS_2 surface,[73] charge trapping at the SiO_2/MoS_2 interface,[74] and intrinsic defects within the MoS_2 material.[75] However, we did not observe any qualitative difference in the nature of hysteresis after the Cu-doping. Figure S4 shows the hysteresis in the transfer characteristics of Cu-doped MoS_2 before and after vacuum annealing at 200 °C for 1 h. No significant change was observed after annealing.

ARTICLE IN PRESS

Figure 3f presents a comparison of I_{DS} versus V_{DS} at V_{GS} = 0 V for both pristine and Cu-doped MoS_2. After Cu doping, the current decreases by ∼ 4 order compared to the pristine MoS_2. Dark current significantly impacts photodetector performance, as reducing it enhances power efficiency and improves photocurrent measurement accuracy by preventing saturation of read-out electronics.[76] Furthermore, dark current is a primary source of electronic noise, directly impacting signal detection efficiency. Consequently, minimizing dark current is essential for optimizing the overall performance of photodetectors. In previous studies, a high negative gate bias has been applied to deplete charge carriers in the channel, effectively reducing dark current and improving the signal-to-noise ratio (SNR).[11,13] However, this approach not only increases power consumption due to the large gate bias but also compromises responsivity, as the photocurrent is lower when the device operates in the depletion region.[77] We further investigated the influence of Cu-doping on the photoresponse properties of MoS_2-based devices. **Figures** 4a and 4b depict the I_{DS} versus V_{DS} characteristics at V_{GS} = 0 V for pristine and Cu-doped MoS_2 devices, respectively, under both light and dark conditions. The pristine MoS_2 device (**Figure** 4a) exhibits an on/off current ratio of approximately 10, which is defined using the Equation 2:[78]

$$\frac{I_{\text{on}}}{I_{\text{off}}} = \frac{I_{\text{light}}}{I_{\text{dark}}} \tag{2}$$

where I_{light} is the current under illumination, and I_{dark} is the current in the dark. After Cu doping, the device demonstrates a significantly higher on/off current ratio of approximately 10^4 (Figure 4b). Figures 4c and 4d illustrate the incident power (P) versus photocurrent (I_{ph}) for the pristine and Cu-doped devices, respectively. The photocurrent is defined using Equation 3

$$I_{\text{ph}} = I_{\text{light}} - I_{\text{dark}} \tag{3}$$

The relationship between photocurrent and incident power can be described by the power

ARTICLE IN PRESS

law equation 4

$$I_{\rm ph} \propto P^{\alpha} \tag{4}$$

For the pristine and Cu-doped MoS_2 devices, the observed α values were 0.57 and 0.96, respectively. An α value of 1 indicates a linear relationship, suggesting that the increase in photocurrent is predominantly due to photogenerated carriers (photoconductive effect).[79] When $\alpha < 1$, it indicates sub-linear behaviour, often attributed to the presence of traps, defects or other complex photogeneration and recombination processes.[80,81]

Figure S5 shows the I_{DS}–V_{GS} transfer characteristics of the Cu-doped MoS_2 device measured under dark and illuminated conditions. Under illumination, the threshold voltage shifts toward more negative gate voltages, which is attributed to the photogating effect, as previously reported for MoS_2 photodetectors.[14,81] We have measured the gate leakage current under the same illumination conditions (shown in Figure S6), and the leakage current was found to be very low.

Figures 4e and 4f show the time-resolved photoresponse of pristine and Cu-doped MoS_2, respectively, under alternating dark and illumination conditions. For pristine sample, a 470 nm light emitting diode (LED) was periodically switched on (30 s) and off (30 s) at different power levels. For Cu-doped MoS_2, the LED was switched on and off for 10 s. With increasing incident power, both types of samples exhibited an increase in current. For pristine MoS_2, the dark current is around 10 nA, and the change in current under illumination is less than one order of magnitude. In contrast, for Cu-doped MoS_2, the dark current is approximately 0.1 pA, and the change in current under illumination is four orders of magnitude. Additionally, the cyclic endurance of two devices before and after Cu-doping has been presented in Figures S7 and S8. In the case of pristine MoS_2, the current does not return to its initial value after the LED is switched off during each cycle. This slow decay is likely due to the persistent photoconductivity effect, which arises from the trapping of minority carriers (holes) in localized defect states within MoS_2 or at the MoS_2-substrate interface.[9–12] In contrast, the Cu-doped device demonstrates consistency and stable photoswitching performance over cycles and

ARTICLE IN PRESS

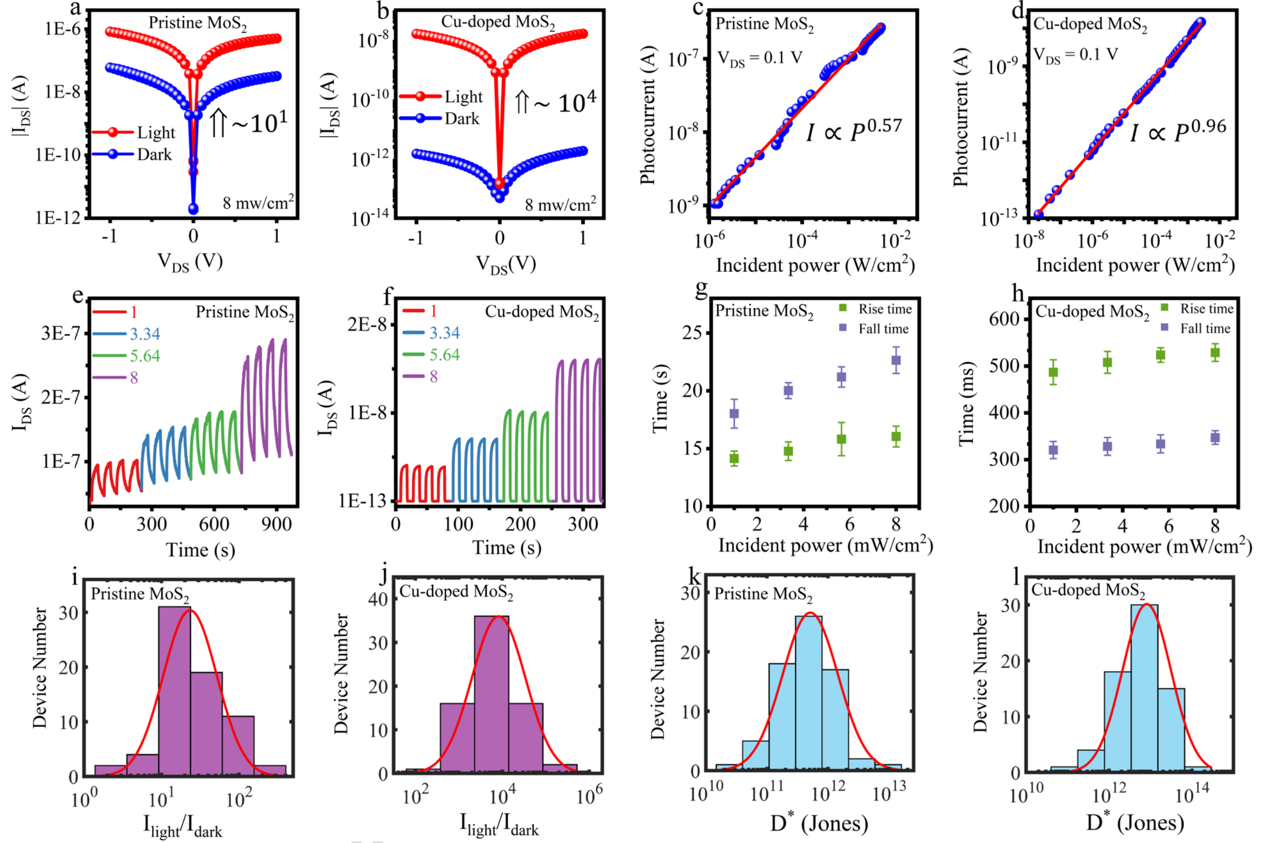

Figure 4: **Opto-electronic properties of pristine and Cu-doped MoS_2.** (a) I_{DS} versus V_{DS} characteristics at $V_{GS} = 0$ V for pristine MoS_2 device, under both light and dark conditions (b)I_{DS} versus V_{DS} characteristics at $V_{GS} = 0$ V for Cu-doped MoS_2, under both light and dark conditions (c) photocurrent versus incident power for pristine MoS_2, red line shows the power law ($I_{ph} \propto P^{\alpha}$) fitting with $\alpha = 0.57$. (d) photocurrent versus incident power for Cu-doped MoS_2, red line shows the power law fitting with $\alpha = 0.96$.. (e) Time-resolved photoresponse of pristine MoS_2 under alternating dark and illumination conditions at different incident powers. A 470 nm LED was periodically turned on and off every 30 seconds. The numbers shown in the inset, color-coded accordingly, indicate the incident power in mW/cm^2. (f) Time-resolved photoresponse of Cu-doped MoS_2 under alternating dark and illumination conditions at different incident powers. A 470 nm LED was periodically turned on and off every 10 seconds. The numbers shown in the inset, color-coded accordingly, indicate the incident power in mW/cm^2. (g) Calculated average rise and fall times at different incident powers for pristine MoS_2. (h) Calculated average rise and fall times at different incident powers for Cu-doped MoS_2. (i) Histogram plot of I_{light}/I_{dark} ratio for pristine MoS_2. The distribution is fitted with a log-normal curve, with a mean $I_{light}/I_{dark} = 10^{1.4}$. (j) Histogram plot of I_{light}/I_{dark} ratio for Cu-doped MoS_2. The distribution is fitted with a log-normal curve, with a mean value of $I_{light}/I_{dark} = 10^{3.9}$ (k) Histogram plot of specific detectivity (D*) of pristine MoS_2 with a average value of detectivity $10^{11.7}$ jones. (l) Histogram of D* for Cu-doped MoS_2 exhibiting an average value of detectivity of $10^{12.9}$ jones.

ARTICLE IN PRESS

quickly reverts to its initial dark conductivity once the light source is turned off. Furthermore, we have analysed the response time using time-resolved photoresponse. The response time of a photodetector is a key parameter for assessing its sensitivity to light signals, indicating how quickly it reacts to changes in light intensity. The rise time (τ_{rise}) is defined as the duration for the photocurrent to increase from 10% to 90% of its peak value, while the fall time (τ_{fall}) represents the duration for the photocurrent to decrease from 90% to 10% of its peak. Figures 4g and 4h present the calculated average rise and fall times at various light intensities, for pristine and Cu-doped MoS_2, respectively. For pristine MoS_2, average rise time increases slightly from approximately 14 to 16 s, while the fall time increases from 18 to 22 s as light intensity increases. This behaviour may be attributed to the presence of trap states in the material. In comparison, Cu-doped MoS_2 (Figure 4h) exhibits a much faster response, with the average rise times ranging from 487 to 529 ms and fall times of 320 to 347 ms. Figures 4i and 4j present a statistical study of 70 devices fabricated with identical geometry (Figure S3, channel length 4 μm and width 10 μm), illustrating a log-normal distribution of the $I_{\text{light}}/I_{\text{dark}}$ ratio before and after Cu-doping. Before doping (Figure 4i), most devices exhibit a ratio in the range of 10^1-10^2. While after Cu-doping (Figure 4j), the majority of devices show a significantly higher ratio, reaching approximately 10^4. Figures S8 to S14 show a comparison of dark current and time-resolved photoresponse of six representative devices before and after Cu doping, clearly illustrating the improved photoresponse and suppressed dark current after doping. Figure S15 further supports this trend with a histogram of dark current values. Before doping, the majority of devices exhibit dark currents exceeding 1 nA, whereas after doping, most devices show a substantial reduction, with values predominantly in the 0.1–10 pA range. The Specific detectivity (D*) for each device was also evaluated, which is an important figure of merit for photodetectors, representing the sensitivity level of the device. The specific detectivity is calculated using Equation (5)

$$D^* = R \times \left(\frac{2eI_{\text{dark}}}{A}\right)^{-1/2} \tag{5}$$

ARTICLE IN PRESS

where R is the responsivity, A is the device area, q is the electronic charge, and I_{dark} is the dark current. Figures 4k and 4l present histograms of the specific detectivity for pristine and Cu-doped MoS_2, respectively. For pristine MoS_2, the majority of devices show detectivity in the range of 10^{11} to 10^{12} jones, while for Cu-doped MoS_2, most devices exhibit detectivity in the range of 10^{12} to 10^{14} jones. Furthermore, to assess device-to-device variability and the effect of Cu doping on transistor performance, Figures S16–S19 show the distributions of I_{ON}, μ_{FE}, V_{TH}, and SS before and after Cu-doping.

To gain further insight into the photoresponse, the transient curves of pristine and Cu-doped MoS_2 were fitted using an exponential function with two decay times, as shown in Equation 6. Here A_1 and A_2 represent the trap coefficients for the exponential curve. The faster decay component is attributed to shallow traps, while the slower decay component corresponds to deep traps.[82] **Figure** 5a illustrates the schematic of the band structure of an n-type semiconductor with trap and recombination center. For simplicity, one shallow trap, one deep trap, and one recombination centers are considered.

$$I = I_0 + A_1 e^{-t/\tau_1} + A_2 e^{-t/\tau_2} \tag{6}$$

Localized states within the bandgap can act as a recombination center, shallow trap or deep trap, depending on their position in the bandgap and the Fermi level.[23,83] Previous studies have shown that band tail states are present in the conduction and valence bands of MoS_2.[9,84] In addition to these shallow traps, deep traps and recombination centers are also present.[9,84] These trap states are caused by structural defects in MoS_2 such as vacancies and grain boundaries, or by a distribution of trap charges introduced by the MoS_2–SiO_2 interface.[9,82,84–86] Furthermore, sulfur vacancies in MoS_2 have been reported to introduce both deep and shallow level traps, but the trap density is higher at the deep level.[82] Figure 5b shows the transient response of pristine MoS_2, along with the fitted curve. The extracted decay times (τ_1 and τ_2) and trap coefficients (A_1 and A_2) are summarized in supplementary

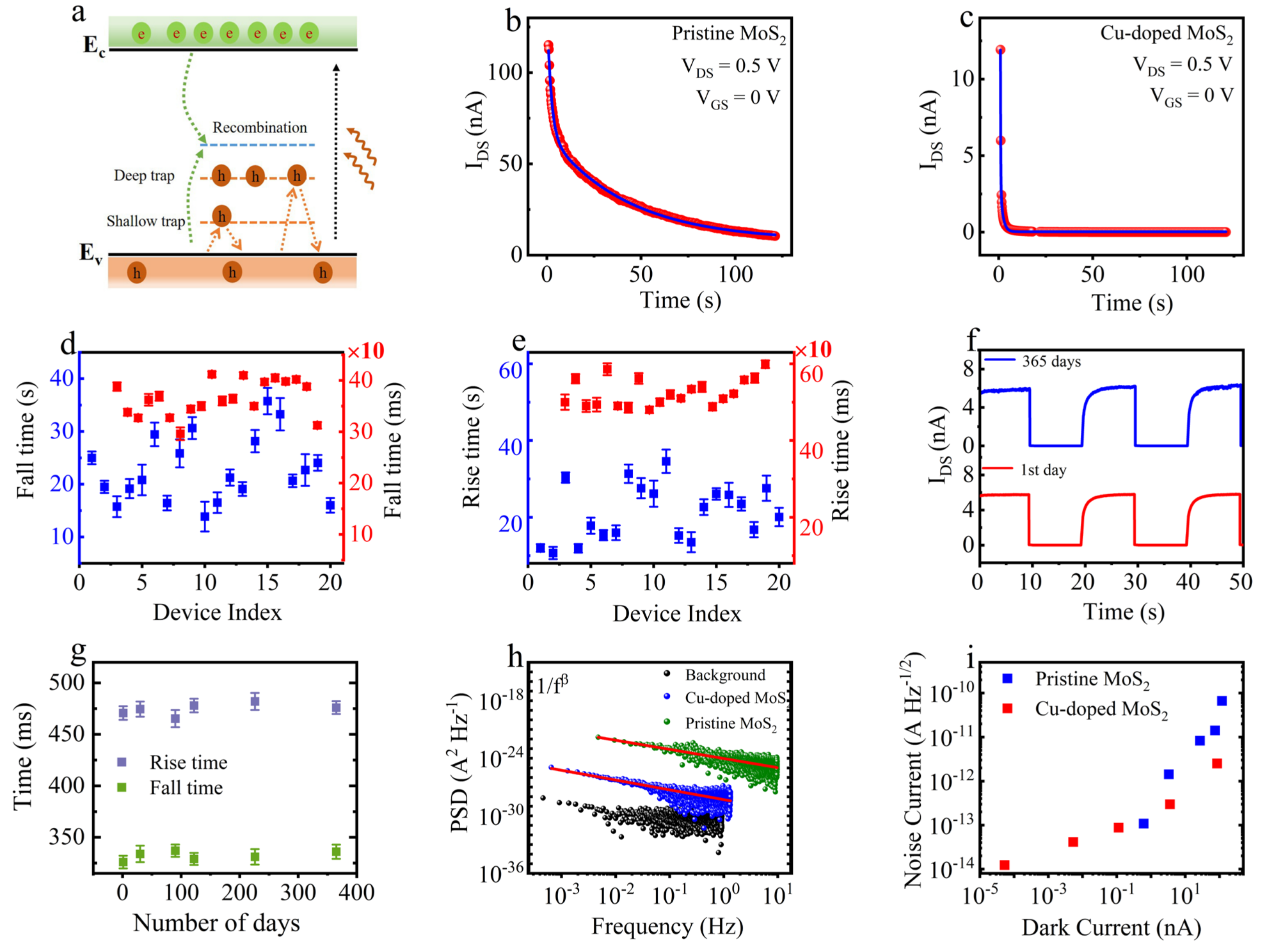

Figure 5: (a) Schematic diagram of the band structure of an n-type semiconductor showing representative trap and recombination centers. For clarity, one shallow trap, one deep trap, and a single recombination center are included. (b) Decay curve of pristine MoS_2 at V_{DS} = 0.5 V and V_{GS} = 0 V (c) decay curve of Cu-doped MoS_2 under the same bias conditions. (d) Average fall time for 20 devices before and after doping. (e) Average rise time for 20 devices before and after doping. (f) Time-resolved photoresponse of Cu-doped device under alternating dark and illuminated conditions (on/off time 10 s and illumination power = 8 mW cm^{-2} and bias condition at V_{DS} = 0.5 V and V_{GS} = 0 V) after 1 day and 365 days. (g) Average rise and fall time for various days from 1st to 365 days. (h) Noise spectral density as a function of frequency under ambient conditions. The black dots represent the background noise, while the green and blue dots correspond to the noise spectra before and after doping, respectively, at V_{DS} = 0.5 V. The red line shows the $1/f^{\beta}$ fitting, with $\beta = 0.95$ before doping and $\beta = 1.05$ after doping. (i) Dark current versus noise current for pristine MoS_2 and Cu-doped MoS_2.

ARTICLE IN PRESS

table 1. Before Cu doping, the contribution from deep traps was significant. The de-trapping time of carriers from deep traps can be longer by several orders of magnitude compared to shallow traps, leading to an extended decay or response time of the device. Figure 5c shows the transient response of Cu-doped MoS_2, where the contribution from shallow traps becomes dominant compared to deep traps, leading to a faster photoresponse. Similarly, in ReS_2-based photodetectors, photoresponse speed has been improved by modulating deep traps to shallow traps using defect engineering.[23] Further analysis of fall and rise time was carried out for 20 devices before and after doping. Figure 5d illustrates the distribution of fall times before and after doping. Before doping, the fall time varies between 13 and 35 s, as indicated by the blue data points on the left y-axis. After Cu doping, a substantial reduction in fall time is observed, with values ranging from 296 to 412 ms (red data points, right y-axis). A similar trend is evident in the rise time behaviour, as shown in Figure 5e. Before doping, the rise time ranges from 10 to 30 s (blue data points, left y-axis), whereas after doping it decreases significantly to 480 to 600 ms (red data points, right y-axis). Additionally, the long-term operational stability of the device was assessed by monitoring its time-resolved photoresponse over an extended duration. Figure 5f presents the photoresponse measured on day 1 and after 365 days. The results show negligible degradation in photocurrent amplitude or dynamics, indicating robust stability of the device under ambient storage conditions. To further quantify this, the corresponding rise and fall times over different time points are plotted in Figure 5g. The absence of any significant variation in these parameters confirms the excellent temporal stability and reproducibility of the photoresponse in Cu-doped MoS_2 devices. Next, we have evaluated the current noise power spectral density (PSD) of both the pristine and Cu-doped MoS_2 devices. Figure 5h shows the noise spectra as a function of frequency, revealing characteristic $1/f^{\beta}$ behaviour with exponents $\beta = 0.95$ (before doping) and $\beta = 1.05$ (after doping). However, noise detection above 10 Hz was limited by the instrument's resolution, as shown in Figure 5h. We measured the background noise (black dots), which remained lower than the device noise both before (green dots) and after (blue

ARTICLE IN PRESS

dots) doping. The differing frequency ranges observed in the three spectra are due to the instrument's resolution, which varies depending on the measured current range. We estimated the specific detectivity of the devices using the measured noise spectra and Equation 7

$$D^* = \frac{\sqrt{AB}R}{i_n} \tag{7}$$

where A is the area of device, R is the responsivity, B is the bandwidth and i_n is the noise current. For our device $A = 40\ \mu m^2$ and $B = 1\ Hz$. The measured noise current decreased significantly from 1.03×10^{-12} A $Hz^{-1/2}$ in the pristine device to 1.13×10^{-14} A $Hz^{-1/2}$ after doping. Correspondingly, the calculated specific detectivity improved from 2.4×10^{10} cm Hz W^{-1} to 3.5×10^{13} cm Hz W^{-1}. Additionally, Figure 5i illustrates the variation of noise current with respect to dark current. An overall increasing trend in noise current is observed with higher dark current levels. Notably, after Cu doping, the noise current is consistently lower than that of the pristine device. Additionally, Figures S12a and S12b compare the shot noise limit with noise current at different dark current levels.

In Table 2 we have presented a comparison of key photodetection metrics for our MoS_2 devices with representative previous works.[5,13,87,88] Overall, these results demonstrate that the optoelectronic performance of monolayer MoS_2 improves significantly after morphotaxial Cu doping.

ARTICLE IN PRESS

ARTICLE IN PRESS

Table 2: **Comparison of photodetector performance of MoS_2-based devices.**

cccccccccc

Ref	Channel	Area	λ (nm)	P_{in} (mw/cm^2)	R (A/W)	D* (jones)	NEP (V
[87]	MoS_2	1μm × 5μm	450-625	2	3.6×10^7	5.6×10^{13}	–
[5]	MoS_2	2.1μm × 2.6μm	450	–	4.2×10^{-4}	–	–
[13]	MoS_2	–	561	0.024	881	–	1.8 ×
[88]	MoS_2	–	470	10	17.4	2.48×10^{12}	–
This work	Pristine MoS_2	4 μm × 10 μm	470	8	313	2.4×10^{10}	1.6 ×
This work	Cu-doped MoS_2	4 μm × 10 μm	470	8	15.6	3.5×10^{13}	6.4 ×

ARTICLE IN PRESS

Conclusion

In summary, we demonstrate that solvent-mediated morphotaxial cation exchange enables substitutional Cu incorporation in CVD-grown monolayer MoS_2 while preserving the crystal morphology. Beyond inducing stable p-type behavior, this lattice-level doping fundamentally

ARTICLE IN PRESS

modifies the electronic defect landscape of MoS_2. The Cu-doped monolayers exhibit a dramatic suppression of dark current, resulting in nearly three orders of magnitude increase in the light-to-dark current ratio and more than an order of magnitude faster photoresponse. Transient and noise analyses reveal that these improvements arise from the reduction of deep trap states and the associated suppression of trap-assisted carrier fluctuations, establishing substitutional doping as an effective route for trap-state engineering rather than simple carrier density modulation.

In the absence of gate bias, the dark current in doped devices is reduced by four orders of magnitude compared to pristine devices, further highlighting their improved energy efficiency. As a result, the doped devices achieve detectivity values up to 10^{14} Jones without gate bias, together with excellent operational stability under ambient conditions. These findings introduce morphotaxial substitution as a scalable strategy for electronically modifying monolayer semiconductors and demonstrate that controlled lattice doping can simultaneously address dark current, response speed, and noise limitations in 2D photodetectors. More broadly, this work highlights substitutional chemistry as a powerful tool for tailoring defect physics and advancing the performance limits of atomically thin optoelectronic materials.

ARTICLE IN PRESS

Methods

Growth of monolayer MoS_2

Monolayer MoS_2 was synthesized on 285 nm SiO_2 coated Si substrates via atmospheric pressure chemical vapor deposition (APCVD). Sulfur (Sigma-Aldrich) and molybdenum trioxide MoO_3, 99.98% trace metals, Sigma-Aldrich) powders were used as sulfur and molybdenum sources, respectively. The substrates were first cleaned through sequential sonication in acetone and isopropyl alcohol, each for 10 minutes, and then subjected to oxygen plasma treatment at ~400 mTorr for 5 minutes using a 40 W RF source. During the growth process, 400 mg of sulfur powder (towards the outside furnace) was placed in an alumina boat positioned

ARTICLE IN PRESS

about 18 cm upstream from the MoO_3 boat, in a 3.5 cm diameter quartz tube furnace. A heating belt was employed to control the sulfur temperature independently. The cleaned substrates were placed downstream from the MoO_3 boat, approximately 5 cm apart, in a separate alumina boat. Before heating, the system was purged with ultrahigh-purity argon gas at 400 sccm for 15 minutes, then reduced to 20 sccm for the remainder of the process. The furnace was ramped to 700°C at 5°C/min and held for 5 minutes before allowing it to cool naturally. Meanwhile, sulfur was heated to 150°C using the heating belt as the furnace approached its target temperature, and this temperature was maintained for 25 minutes before cooling.

Material Characterization

Raman and Photoluminescence Spectroscopy

Raman and PL spectra were collected using a LabRAM HR, Horiba Jobin Yvon spectrometer with a 532 nm laser.

X-ray Photoelectron spectroscopy(XPS)

X-ray photoelectron spectroscopy (XPS) was performed using a Thermo Scientific XPS instrument, which was equipped with a monochromatic Kα Al X-ray line as the X-ray source. The X-ray beam had an approximate diameter of 400 μm and an energy of 1486.6 eV. To counter sample charging, all spectra underwent charge correction against the C 1s adventitious carbon peak at 284.8 eV.

High-Resolution Transmission Electron Microscopy (HRTEM)

High-resolution transmission electron microscopy (HRTEM) images were acquired using a JEOL HRTEM instrument, JEM-2200FS, and the microscopes were employed with an acceleration voltage of 200 kV.

ARTICLE IN PRESS

ARTICLE IN PRESS

Kelvin Probe Force Microscopy (KPFM)

KPFM measurements were done using an Asylum Research MFP-3D Origin^{+} instrument in non-contact mode.

Device fabrication and Opto-electrical Measurement

Devices were fabricated using a standard photolithography method followed by thermal evaporation of metal (5nm Cr and 50nm Au) and lift-off in acetone. All electrical measurements were performed in a home-built probe station using a Keithley 2636B dual-channel source meter unit and home-built LabVIEW programs at ambient conditions. A 470 nm LED, connected in series and controlled by an Arduino, was employed as the light source for measuring photoresponse. The optical power was calibrated at the device plane using a Thorlabs power meter.

ARTICLE IN PRESS

Data availability

The data that support the findings of this study are available from the corresponding author upon reasonable request.

Acknowledgement

The authors acknowledge funding support from a DST SERB grant no. CRG/2021/005659, and partial support from the National Mission on Interdisciplinary Cyber-Physical Systems (NM-ICPS) of the DST, Government of India, through the I-HUB Quantum Technology Foundation, Pune, India. Manisha Rajput acknowledges DST, Government of India, for the INSPIRE fellowship (IF190124). Manisha Rajput acknowledges Sudipta Majumder and Ankit Kumar for their valuable suggestions.

ARTICLE IN PRESS

Author contributions

M.R. and A.R. conceived and designed the experiments. M.R. and S.B. synthesised the samples. M.R. performed the electrical measurements and analysed the data. M.R., G.V.P.K., and A.R. wrote the manuscript. A.S. conducted the optical measurements. A.M. performed the KPFM measurements. A.M. and S.B. analysed the KPFM data. All authors discussed the results and contributed to the final version of the manuscript.

Competing interests

The authors declare no competing interests.

ARTICLE IN PRESS

References

(1) Mak, K. F.; Lee, C.; Hone, J.; Shan, J.; Heinz, T. F. Atomically thin MoS 2: a new direct-gap semiconductor. *Physical review letters* **2010**, *105*, 136805.

(2) Radisavljevic, B.; Radenovic, A.; Brivio, J.; Giacometti, V.; Kis, A. Single-layer MoS2 transistors. *Nature nanotechnology* **2011**, *6*, 147–150.

(3) Sundaram, R.; Engel, M.; Lombardo, A.; Krupke, R.; Ferrari, A.; Avouris, P.; Steiner, M. Electroluminescence in single layer MoS2. *Nano letters* **2013**, *13*, 1416–1421.

(4) Majumder, S.; Lohkna, S.; Walve, V.; Chand, R.; Anilkumar, G. M.; Hwang, S.; Pavan Kumar, G.; Deshpande, A.; Ghosh, P.; Rahman, A. Unveiling the Correlation between Defects and High Mobility in MoS2 Monolayers. *ACS Applied Materials & Interfaces* **2025**, *17*, 10942–10953.

(5) Yin, Z.; Li, H.; Li, H.; Jiang, L.; Shi, Y.; Sun, Y.; Lu, G.; Zhang, Q.; Chen, X.; Zhang, H. Single-layer MoS2 phototransistors. *ACS nano* **2012**, *6*, 74–80.

ARTICLE IN PRESS

(6) Choi, W.; Cho, M. Y.; Konar, A.; Lee, J. H.; Cha, G.-B.; Hong, S. C.; Kim, S.; Kim, J.; Jena, D.; Joo, J., et al. High-detectivity multilayer MoS2 phototransistors with spectral response from ultraviolet to infrared. *Advanced materials* **2012**, *24*, 5832.

(7) Lee, H. S.; Min, S.-W.; Chang, Y.-G.; Park, M. K.; Nam, T.; Kim, H.; Kim, J. H.; Ryu, S.; Im, S. MoS2 nanosheet phototransistors with thickness-modulated optical energy gap. *Nano letters* **2012**, *12*, 3695–3700.

(8) Tsai, M.-L.; Su, S.-H.; Chang, J.-K.; Tsai, D.-S.; Chen, C.-H.; Wu, C.-I.; Li, L.-J.; Chen, L.-J.; He, J.-H. Monolayer MoS2 heterojunction solar cells. *ACS nano* **2014**, *8*, 8317–8322.

(9) Furchi, M. M.; Polyushkin, D. K.; Pospischil, A.; Mueller, T. Mechanisms of Photoconductivity in Atomically Thin MoS2. *Nano Letters* **2014**, *14*, 6165–6170, PMID: 25299515.

(10) Lee, Y.; Yang, J.; Lee, D.; Kim, Y.-H.; Park, J.-H.; Kim, H.; Cho, J. H. Trap-induced photoresponse of solution-synthesized MoS2. *Nanoscale* **2016**, *8*, 9193–9200.

(11) Kufer, D.; Konstantatos, G. Highly Sensitive, Encapsulated MoS2 Photodetector with Gate Controllable Gain and Speed. *Nano Letters* **2015**, *15*, 7307–7313, PMID: 26501356.

(12) George, A.; Fistul, M. V.; Gruenewald, M.; Kaiser, D.; Lehnert, T.; Mupparapu, R.; Neumann, C.; Hübner, U.; Schaal, M.; Masurkar, N.; Arava, L. M. R.; Staude, I.; Kaiser, U.; Fritz, T.; Turchanin, A. Giant persistent photoconductivity in monolayer MoS2 field-effect transistors. *npj 2D Materials and Applications* **2021**, *5*, 15.

(13) Lopez-Sanchez, O.; Lembke, D.; Kayci, M.; Radenovic, A.; Kis, A. Ultrasensitive photodetectors based on monolayer MoS2. *Nature Nanotechnology* **2013**, *8*, 497–501.

(14) Bartolomeo, A. D.; Genovese, L.; Foller, T.; Giubileo, F.; Luongo, G.; Croin, L.; Liang, S.-

ARTICLE IN PRESS

ARTICLE IN PRESS

J.; Ang, L. K.; Schleberger, M. Electrical transport and persistent photoconductivity in monolayer MoS2 phototransistors. *Nanotechnology* **2017**, *28*, 214002.

(15) Zhang, W.; Huang, J.-K.; Chen, C.-H.; Chang, Y.-H.; Cheng, Y.-J.; Li, L.-J. High-Gain Phototransistors Based on a CVD MoS2 Monolayer. *Advanced Materials* **2013**, *25*, 3456–3461.

(16) Zhou, X.; Zhou, N.; Li, C.; Song, H.; Zhang, Q.; Hu, X.; Gan, L.; Li, H.; Lü, J.; Luo, J., et al. Vertical heterostructures based on SnSe2/MoS2 for high performance photodetectors. *2D Materials* **2017**, *4*, 025048.

(17) Adinolfi, V.; Sargent, E. H. Photovoltage field-effect transistors. *Nature* **2017**, *542*, 324–327.

(18) Kufer, D.; Nikitskiy, I.; Lasanta, T.; Navickaite, G.; Koppens, F.; Konstantatos, G. Hybrid 2D-0D MoS2-PbS quantum dot photodetectors. *Advanced Materials (Deerfield Beach, Fla.)* **2014**, *27*, 176–180.

(19) Xu, D.; Jian, P.; Liu, W.; Tan, S.; Yang, Y.; Peng, M.; Dai, J.; Chen, C.; Wu, F. Vanadium Metal Doping of Monolayer MoS2 for p-Type Transistors and Fast-Speed Phototransistors. *ACS Applied Materials & Interfaces* **2024**, *16*, 23771–23779.

(20) Ghosh, S.; Sadaf, M. U. K.; Graves, A. R.; Zheng, Y.; Pannone, A.; Ray, S.; Cheng, C.-Y.; Guevara, J.; Redwing, J. M.; Das, S. High-performance p-type bilayer WSe2 field effect transistors by nitric oxide doping. *Nature Communications* **2025**, *16*, 5649.

(21) Das, M.; Sen, D.; Sakib, N. U.; Ravichandran, H.; Sun, Y.; Zhang, Z.; Ghosh, S.; Venkatram, P.; Subbulakshmi Radhakrishnan, S.; Sredenschek, A., et al. High-performance p-type field-effect transistors using substitutional doping and thickness control of two-dimensional materials. *Nature Electronics* **2025**, *8*, 24–35.

ARTICLE IN PRESS

ARTICLE IN PRESS

(22) Pan, Y.; Jian, T.; Gu, P.; Song, Y.; Wang, Q.; Han, B.; Ran, Y.; Pan, Z.; Li, Y.; Xu, W., et al. Precise p-type and n-type doping of two-dimensional semiconductors for monolithic integrated circuits. *Nature Communications* **2024**, *15*, 9631.

(23) Jiang, J.; Ling, C.; Xu, T.; Wang, W.; Niu, X.; Zafar, A.; Yan, Z.; Wang, X.; You, Y.; Sun, L.; Lu, J.; Wang, J.; Ni, Z. Defect Engineering for Modulating the Trap States in 2D Photoconductors. *Advanced Materials* **2018**, *30*, 1804332.

(24) Ross, J. S.; Klement, P.; Jones, A. M.; Ghimire, N. J.; Yan, J.; Mandrus, D.; Taniguchi, T.; Watanabe, K.; Kitamura, K.; Yao, W., et al. Electrically tunable excitonic light-emitting diodes based on monolayer WSe2 p–n junctions. *Nature nanotechnology* **2014**, *9*, 268–272.

(25) Zhang, Y. J.; Ye, J. T.; Yomogida, Y.; Takenobu, T.; Iwasa, Y. Formation of a Stable p–n Junction in a Liquid-Gated MoS2 Ambipolar Transistor. *Nano Letters* **2013**, *13*, 3023–3028, PMID: 23795701.

(26) Sun, R.; Sun, S.; Liang, X.; Gong, H.; Zhang, X.; Li, Y.; Gao, M.; Li, D.; Xu, G. Surface charge transfer doping of MoS2 monolayer by molecules with aggregation-induced emission effect. *Nanomaterials* **2022**, *12(1)*, 164.

(27) Cho, Y.; Park, J. H.; Kim, M.; Jeong, Y.; Yu, S.; Lim, J. Y.; Yi, Y.; Im, S. Impact of organic molecule-induced charge transfer on operating voltage control of both n-MoS2 and p-MoTe2 transistors. *Nano letters* **2019**, *19*, 2456–2463.

(28) Lockhart de la Rosa, C. J.; Phillipson, R.; Teyssandier, J.; Adisoejoso, J.; Balaji, Y.; Huyghebaert, C.; Radu, I.; Heyns, M.; De Feyter, S.; De Gendt, S. Molecular doping of MoS2 transistors by self-assembled oleylamine networks. *Applied Physics Letters* **2016**, *109*, 253112.

(29) Fan, S.; Tang, X.; Zhang, D.; Hu, X.; Liu, J.; Yang, L.; Su, J. Ambipolar and n/p-type

ARTICLE IN PRESS

ARTICLE IN PRESS

conduction enhancement of two-dimensional materials by surface charge transfer doping. *Nanoscale* **2019**, *11*, 15359–15366.

(30) Min, S.-W.; Yoon, M.; Yang, S. J.; Ko, K. R.; Im, S. Charge-transfer-induced p-type channel in MoS2 flake field effect transistors. *Acs Applied Materials & Interfaces* **2018**, *10*, 4206–4212.

(31) Gao, H.; Suh, J.; Cao, M. C.; Joe, A. Y.; Mujid, F.; Lee, K.-H.; Xie, S.; Poddar, P.; Lee, J.-U.; Kang, K., et al. Tuning electrical conductance of MoS2 monolayers through substitutional doping. *Nano Letters* **2020**, *20*, 4095–4101.

(32) Loh, L.; Zhang, Z.; Bosman, M.; Eda, G. Substitutional doping in 2D transition metal dichalcogenides. *Nano Research* **2021**, *14*, 1668–1681.

(33) Kanahashi, K.; Tanaka, I.; Nishimura, T.; Aso, K.; Lu, A. K. A.; Morito, S.; Chen, L.; Kakeya, T.; Watanabe, S.; Oshima, Y., et al. Dimensionality-Induced Transition from Degenerate to Nondegenerate States in Nb-Doped WSe2. *ACS nano* **2025**, *19(10)*, 10244–10254.

(34) Suh, J.; Park, T.-E.; Lin, D.-Y.; Fu, D.; Park, J.; Jung, H. J.; Chen, Y.; Ko, C.; Jang, C.; Sun, Y., et al. Doping against the native propensity of MoS2: degenerate hole doping by cation substitution. *Nano letters* **2014**, *14(12)*, 6976–6982.

(35) Das, S.; Demarteau, M.; Roelofs, A. Nb-doped single crystalline MoS2 field effect transistor. *Applied Physics Letters* **2015**, *106*, 173506.

(36) Torsi, R.; Munson, K. T.; Pendurthi, R.; Marques, E.; Van Troeye, B.; Huberich, L.; Schuler, B.; Feidler, M.; Wang, K.; Pourtois, G., et al. Dilute rhenium doping and its impact on defects in MoS2. *ACS nano* **2023**, *17*, 15629–15640.

(37) Doping in 2D. *Nature Electronics* **2021**, *4*, 699–699.

ARTICLE IN PRESS

ARTICLE IN PRESS

(38) Sahoo, K. R.; Panda, J. J.; Bawari, S.; Sharma, R.; Maity, D.; Lal, A.; Arenal, R.; Rajalaksmi, G.; Narayanan, T. N. Enhanced room-temperature spin-valley coupling in V-doped MoS_2. *Phys. Rev. Mater.* **2022**, *6*, 085202.

(39) Zou, J.; Cai, Z.; Lai, Y.; Tan, J.; Zhang, R.; Feng, S.; Wang, G.; Lin, J.; Liu, B.; Cheng, H.-M. Doping concentration modulation in vanadium-doped monolayer molybdenum disulfide for synaptic transistors. *ACS nano* **2021**, *15*, 7340–7347.

(40) Ghosh, S.; Zheng, Y.; Rafiq, M.; Ravichandran, H.; Sun, Y.; Chen, C.; Goswami, M.; Sakib, N. U.; Sadaf, M. U. K.; Pannone, A., et al. A complementary two-dimensional material-based one instruction set computer. *Nature* **2025**, *642*, 327–335.

(41) Kozhakhmetov, A.; Stolz, S.; Tan, A. M. Z.; Pendurthi, R.; Bachu, S.; Turker, F.; Alem, N.; Kachian, J.; Das, S.; Hennig, R. G., et al. Controllable p-type doping of 2D WSe2 via vanadium substitution. *Advanced Functional Materials* **2021**, *31*, 2105252.

(42) Lam, D.; Lebedev, D.; Hersam, M. C. Morphotaxy of Layered van der Waals Materials. *ACS Nano* **2022**, *16*, 7144–7167, PMID: 35522162.

(43) Kerwin, B. P.; Lee, J. H.; Utama, M. I. B.; Pham, T. T.; Pereyra, A.; Sangwan, V. K.; Dravid, V. P.; Facchetti, A.; Hersam, M. C.; Marks, T. J. Morphotaxial Halogenation of Solution-Processed Two-Dimensional Indium Selenide. *Nano Letters* **2025**, *25*, 4734–4742, PMID: 40091587.

(44) Lin, Y.-C.; Bersch, B. M.; Addou, R.; Xu, K.; Wang, Q.; Smyth, C. M.; Jariwala, B.; Walker II, R. C.; Fullerton-Shirey, S. K.; Kim, M. J.; Wallace, R. M.; Robinson, J. A. Modification of the Electronic Transport in Atomically Thin WSe2 by Oxidation. *Advanced Materials Interfaces* **2020**, *7*, 2000422.

(45) Ghasemi, F.; Frisenda, R.; Flores, E.; Papadopoulos, N.; Biele, R.; Perez de Lara, D.; van der Zant, H. S. J.; Watanabe, K.; Taniguchi, T.; D'Agosta, R.; Ares, J. R.;

ARTICLE IN PRESS

ARTICLE IN PRESS

Sánchez, C.; Ferrer, I. J.; Castellanos-Gomez, A. Tunable Photodetectors via In Situ Thermal Conversion of TiS3 to TiO2. *Nanomaterials* **2020**, *10*.

(46) Tian, Z.; Zhao, M.; Xue, X.; Xia, W.; Guo, C.; Guo, Y.; Feng, Y.; Xue, J. Lateral Heterostructures Formed by Thermally Converting n-Type SnSe2 to p-Type SnSe. *ACS Applied Materials & Interfaces* **2018**, *10*, 12831–12838, PMID: 29569894.

(47) Rajput, M.; Mallik, S. K.; Chatterjee, S.; Shukla, A.; Hwang, S.; Sahoo, S.; Kumar, G. P.; Rahman, A. Defect-engineered monolayer MoS 2 with enhanced memristive and synaptic functionality for neuromorphic computing. *Communications Materials* **2024**, *5*, 190.

(48) Koski, K. J.; Cha, J. J.; Reed, B. W.; Wessells, C. D.; Kong, D.; Cui, Y. High-Density Chemical Intercalation of Zero-Valent Copper into Bi2Se3 Nanoribbons. *Journal of the American Chemical Society* **2012**, *134*, 7584–7587, PMID: 22524598.

(49) Wu, J.; Liu, D.; Zhou, J.-G.; Hagelberg, F.; Park, S. S.; Shvartsburg, A. A. Chemistry in Acetone Complexes of Metal Dications: A Remarkable Ethylene Production Pathway. *The Journal of Physical Chemistry A* **2007**, *111*, 4748–4758, PMID: 17503788.

(50) Lee, C.; Yan, H.; Brus, L. E.; Heinz, T. F.; Hone, J.; Ryu, S. Anomalous Lattice Vibrations of Single- and Few-Layer MoS2. *ACS Nano* **2010**, *4*, 2695–2700, PMID: 20392077.

(51) Chakraborty, B.; Bera, A.; Muthu, D. V. S.; Bhowmick, S.; Waghmare, U. V.; Sood, A. K. Symmetry-dependent phonon renormalization in monolayer MoS_2 transistor. *Phys. Rev. B* **2012**, *85*, 161403.

(52) Hu, A.-M.; ling Wang, L.; Xiao, W.-Z.; Meng, B. Electronic structures and magnetic properties in Cu-doped two-dimensional dichalcogenides. *Physica E: Low-dimensional Systems and Nanostructures* **2015**, *73*, 69–75.

ARTICLE IN PRESS

ARTICLE IN PRESS

(53) Sun, X.; Wang, Z. Adsorption and diffusion of lithium on heteroatom-doped monolayer molybdenum disulfide. *Applied Surface Science* **2018**, *455*, 911–918.

(54) Mak, K. F.; He, K.; Lee, C.; Lee, G. H.; Hone, J.; Heinz, T. F.; Shan, J. Tightly bound trions in monolayer MoS2. *Nature Materials* **2013**, *12*, 207–211.

(55) Li, M.; Yao, J.; Wu, X.; Zhang, S.; Xing, B.; Niu, X.; Yan, X.; Yu, Y.; Liu, Y.; Wang, Y. P-type Doping in Large-Area Monolayer MoS2 by Chemical Vapor Deposition. *ACS Applied Materials & Interfaces* **2020**, *12*, 6276–6282, PMID: 31937099.

(56) Mouri, S.; Miyauchi, Y.; Matsuda, K. Tunable Photoluminescence of Monolayer MoS2 via Chemical Doping. *Nano Letters* **2013**, *13*, 5944–5948, PMID: 24215567.

(57) Zhang, S.; Hill, H. M.; Moudgil, K.; Richter, C. A.; Hight Walker, A. R.; Barlow, S.; Marder, S. R.; Hacker, C. A.; Pookpanratana, S. J. Controllable, Wide-Ranging n-Doping and p-Doping of Monolayer Group 6 Transition-Metal Disulfides and Diselenides. *Advanced Materials* **2018**, *30*, 1802991.

(58) Yang, L.; Majumdar, K.; Liu, H.; Du, Y.; Wu, H.; Hatzistergos, M.; Hung, P. Y.; Tieckelmann, R.; Tsai, W.; Hobbs, C.; Ye, P. D. Chloride Molecular Doping Technique on 2D Materials: WS2 and MoS2. *Nano Letters* **2014**, *14*, 6275–6280, PMID: 25310177.

(59) Lin, J. D.; Han, C.; Wang, F.; Wang, R.; Xiang, D.; Qin, S.; Zhang, X.-A.; Wang, L.; Zhang, H.; Wee, A. T. S.; Chen, W. Electron-Doping-Enhanced Trion Formation in Monolayer Molybdenum Disulfide Functionalized with Cesium Carbonate. *ACS Nano* **2014**, *8*, 5323–5329, PMID: 24785254.

(60) Nipane, A.; Karmakar, D.; Kaushik, N.; Karande, S.; Lodha, S. Few-Layer MoS2 p-Type Devices Enabled by Selective Doping Using Low Energy Phosphorus Implantation. *ACS Nano* **2016**, *10*, 2128–2137, PMID: 26789206.

ARTICLE IN PRESS

ARTICLE IN PRESS

(61) Otamiri, J.; Andersson, S.; Andersson, A. Ammoxidation of toluene by YBa2Cu3O6+x and copper oxides: Activity and XPS studies. *Applied Catalysis* **1990**, *65*, 159–174.

(62) Poulston, S.; Parlett, P.; Stone, P.; Bowker, M. Surface oxidation and reduction of CuO and Cu2O studied using XPS and XAES. *Surf. Interface Anal.* **1996**, *24*, 811–820.

(63) Biesinger, M. C. Advanced analysis of copper X-ray photoelectron spectra. *Surface and Interface Analysis* **2017**, *49*, 1325–1334.

(64) Baker, M.; Gilmore, R.; Lenardi, C.; Gissler, W. XPS investigation of preferential sputtering of S from MoS2 and determination of MoSx stoichiometry from Mo and S peak positions. *Applied Surface Science* **1999**, *150*, 255–262.

(65) Buha, J.; Manna, L. Solid State Intercalation, Deintercalation, and Cation Exchange in Colloidal 2D Bi2Se3 and Bi2Te3 Nanocrystals. *Chemistry of Materials* **2017**, *29*, 1419–1429.

(66) Wang, Y.; Morozov, Y. V.; Zhukovskyi, M.; Chatterjee, R.; Draguta, S.; Tongying, P.; Bryant, B.; Rouvimov, S.; Kuno, M. Transforming Layered to Nonlayered Two-Dimensional Materials: Cation Exchange of SnS2 to Cu2SnS3. *ACS Energy Letters* **2016**, *1*, 175–181.

(67) Zhan, Y.; Shao, Z.; Jiang, T.; Ye, J.; Wu, X.; Zhang, B.; Ding, K.; Wu, D.; Jie, J. Cation exchange synthesis of two-dimensional vertical Cu2S/CdS heterojunctions for photovoltaic device applications. *J. Mater. Chem. A* **2020**, *8*, 789–796.

(68) Wang, Y.; Zhukovskyi, M.; Tongying, P.; Tian, Y.; Kuno, M. Synthesis of Ultrathin and Thickness-Controlled Cu2–xSe Nanosheets via Cation Exchange. *The Journal of Physical Chemistry Letters* **2014**, *5*, 3608–3613, PMID: 26278726.

(69) Xiong, X.; Wu, F.; Ouyang, Y.; Liu, Y.; Wang, Z.; Tian, H.; Dong, M. Oxygen

ARTICLE IN PRESS

ARTICLE IN PRESS

incorporated MoS2 for rectification-mediated resistive switching and artificial neural network. *Advanced Functional Materials* **2024**, *34*, 2213348.

(70) Pendurthi, R.; Sakib, N. U.; Sadaf, M. U. K.; Zhang, Z.; Sun, Y.; Chen, C.; Jayachandran, D.; Oberoi, A.; Ghosh, S.; Kumari, S., et al. Monolithic three-dimensional integration of complementary two-dimensional field-effect transistors. *Nature nanotechnology* **2024**, *19*, 970–977.

(71) Jayachandran, D.; Pendurthi, R.; Sadaf, M. U. K.; Sakib, N. U.; Pannone, A.; Chen, C.; Han, Y.; Trainor, N.; Kumari, S.; Mc Knight, T. V., et al. Three-dimensional integration of two-dimensional field-effect transistors. *Nature* **2024**, *625*, 276–281.

(72) Oberoi, A.; Han, Y.; Stepanoff, S. P.; Pannone, A.; Sun, Y.; Lin, Y.-C.; Chen, C.; Shallenberger, J. R.; Zhou, D.; Terrones, M., et al. Toward high-performance p-type two-dimensional field effect transistors: contact engineering, scaling, and doping. *ACS nano* **2023**, *17*, 19709–19723.

(73) Li, T.; Du, G.; Zhang, B.; Zeng, Z. Scaling behavior of hysteresis in multilayer MoS2 field effect transistors. *Applied Physics Letters* **2014**, *105*, 093107.

(74) Park, Y.; Baac, H. W.; Heo, J.; Yoo, G. Thermally activated trap charges responsible for hysteresis in multilayer MoS2 field-effect transistors. *Applied Physics Letters* **2016**, *108*, 083102.

(75) Shu, J.; Wu, G.; Guo, Y.; Liu, B.; Wei, X.; Chen, Q. The intrinsic origin of hysteresis in MoS2 field effect transistors. *Nanoscale* **2016**, *8*, 3049–3056.

(76) Baeg, K.-J.; Binda, M.; Natali, D.; Caironi, M.; Noh, Y.-Y. Organic Light Detectors: Photodiodes and Phototransistors. *Advanced Materials* **2013**, *25*, 4267–4295.

(77) Kufer, D.; Konstantatos, G. Photo-FETs: Phototransistors Enabled by 2D and 0D Nanomaterials. *ACS Photonics* **2016**, *3*, 2197–2210.

ARTICLE IN PRESS

ARTICLE IN PRESS

(78) Anilkumar, G. M.; Bhakar, M.; Taneja, C.; Hwang, S.; Kumar, G. V. P.; Sheet, G.; Rahman, A. Near Room Temperature Solvothermal Growth of Ferroelectric CsPbBr3 Nanoplatelets with Ultralow Dark Current. *Advanced Materials* **2024**, *36*, 2403875.

(79) Sze, S. M.; Ng, K. K. *Physics of Semiconductor Devices*, 3rd ed.; (Wiley & Sons), 2007.

(80) Island, J. O.; Blanter, S. I.; Buscema, M.; van der Zant, H. S.; Castellanos-Gomez, A. Gate controlled photocurrent generation mechanisms in high-gain In2Se3 phototransistors. *Nano letters* **2015**, *15*, 7853–7858.

(81) Fang, H.; Hu, W. Photogating in low dimensional photodetectors. *Advanced science* **2017**, *4*, 1700323.

(82) Lee, J.; Kim, M. J.; Jeong, B. G.; Kwon, C.; Cha, Y.; Choi, S. H.; Kim, K. K.; Jeong, M. S. Electrical role of sulfur vacancies in MoS2: Transient current approach. *Applied Surface Science* **2023**, *613*, 155900.

(83) Streetman, B. G. Carrier Recombination and Trapping Effects in Transient Photoconductive Decay Measurements. *Journal of Applied Physics* **1966**, *37*, 3137–3144.

(84) Zhu, W.; Low, T.; Lee, Y.-H.; Wang, H.; Farmer, D. B.; Kong, J.; Xia, F.; Avouris, P. Electronic transport and device prospects of monolayer molybdenum disulphide grown by chemical vapour deposition. *Nature communications* **2014**, *5*, 3087.

(85) Ghatak, S.; Ghosh, A. Observation of trap-assisted space charge limited conductivity in short channel MoS2 transistor. *Applied Physics Letters* **2013**, *103*, 122103.

(86) Ghatak, S.; Pal, A. N.; Ghosh, A. Nature of Electronic States in Atomically Thin MoS2 Field-Effect Transistors. *ACS Nano* **2011**, *5*, 7707–7712, PMID: 21902203.

(87) Dodda, A.; Jayachandran, D.; Pannone, A.; Trainor, N.; Stepanoff, S. P.; Steves, M. A.; Radhakrishnan, S. S.; Bachu, S.; Ordonez, C. W.; Shallenberger, J. R., et al. Active

ARTICLE IN PRESS

ARTICLE IN PRESS

pixel sensor matrix based on monolayer MoS2 phototransistor array. *Nature Materials* **2022**, *21*, 1379–1387.

(88) Mallick, S.; Majumder, S.; Maiti, P.; Kesavan, K.; Rahman, A.; Rath, A. Development of Self-Doped Monolayered 2D MoS2 for Enhanced Photoresponsivity. *Small* **2024**, *20*, 2403225.

ARTICLE IN PRESS

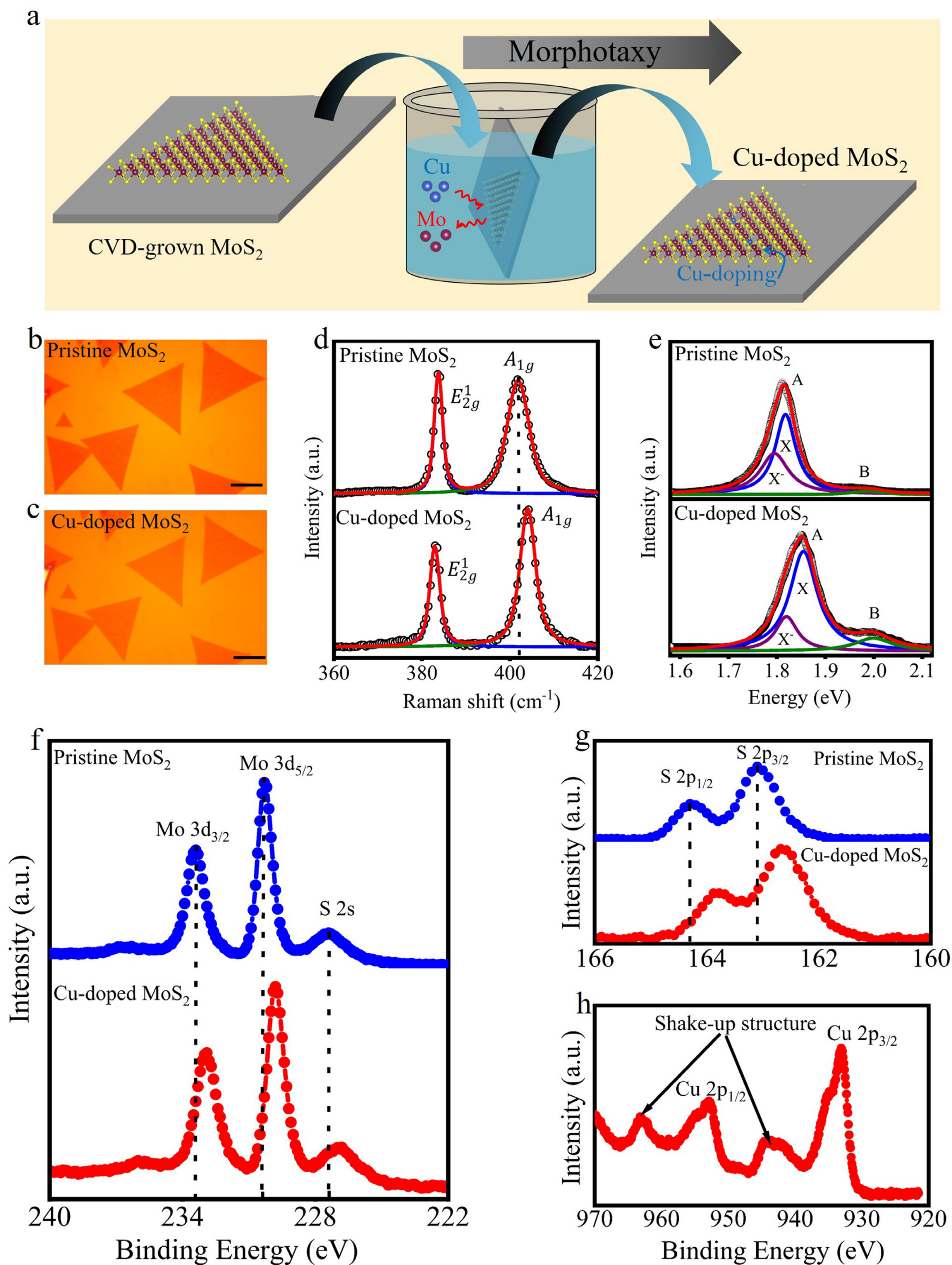
a
Morphotaxy
CVD-grown MoS2
Cu
Mo
Cu-doped MoS2
Cu-doping
b Pristine MoS2
c Cu-doped MoS2
d Pristine MoS2
Cu-doped MoS2
Intensity (a.u.)
Raman shift (cm-1)
e Pristine MoS2
Cu-doped MoS2
Intensity (a.u.)
Energy (eV)
f Pristine MoS2
Mo 3d3/2
Mo 3d5/2
S 2s
Cu-doped MoS2
Intensity (a.u.)
Binding Energy (eV)
g S 2p1/2
S 2p3/2
Pristine MoS2
Cu-doped MoS2
Intensity (a.u.)
h Shake-up structure
Cu 2p3/2
Cu 2p1/2
Intensity (a.u.)
Binding Energy (eV)

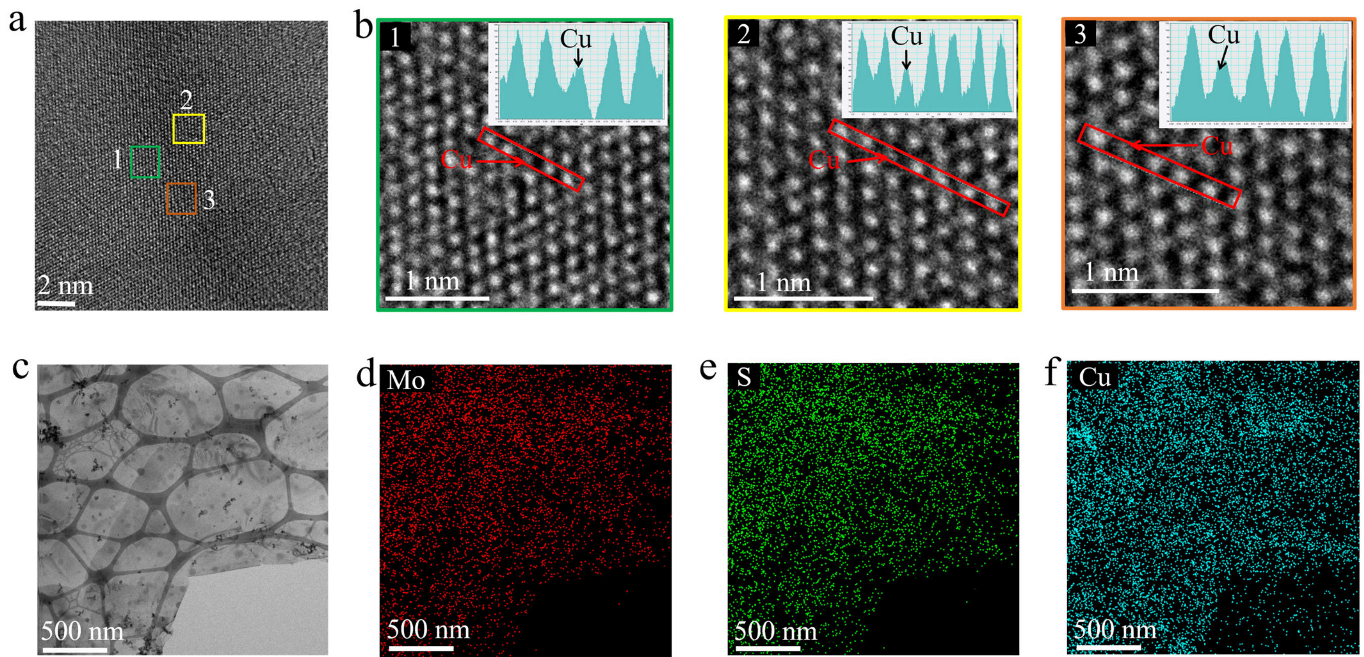

ARTICLE IN PRESS

ARTICLE IN PRESS

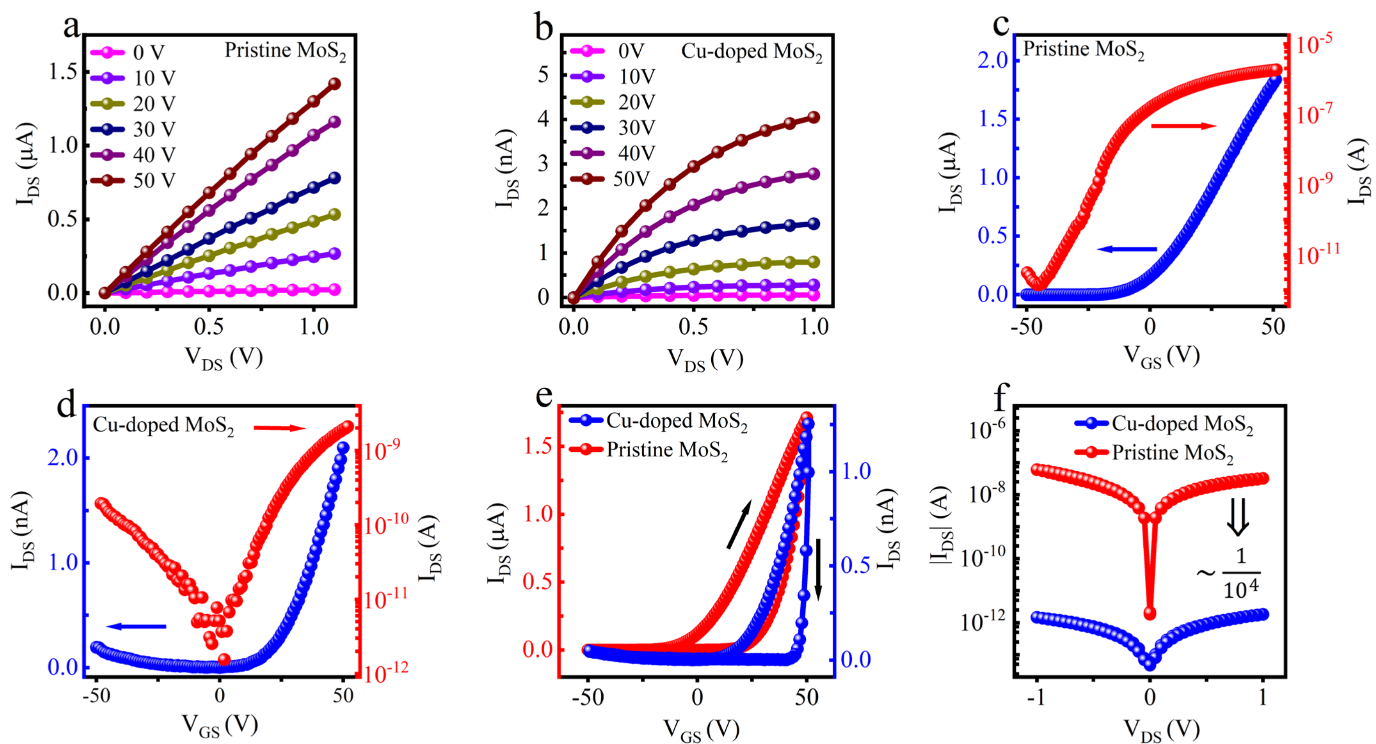

ARTICLE IN PRESS

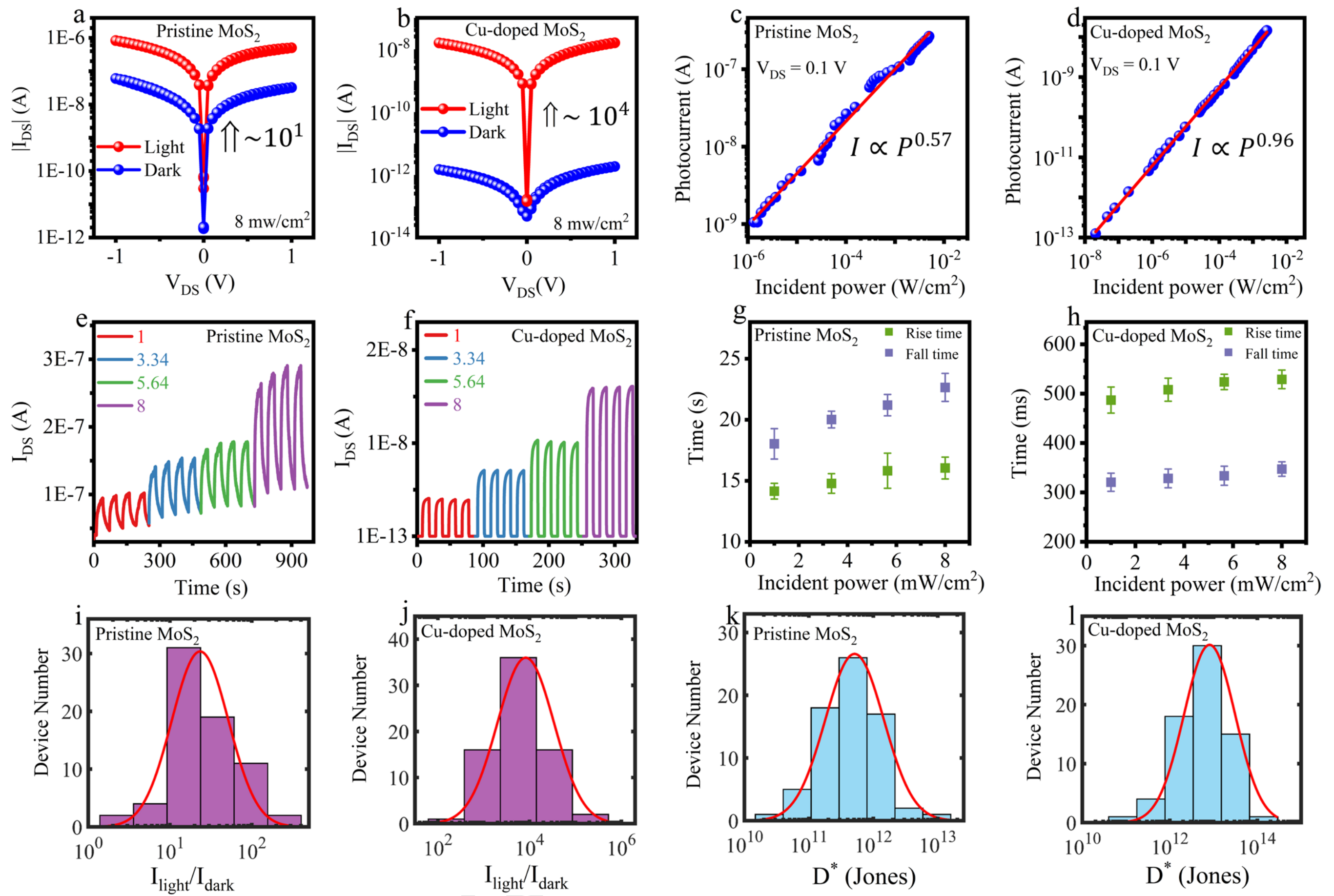

ARTIC

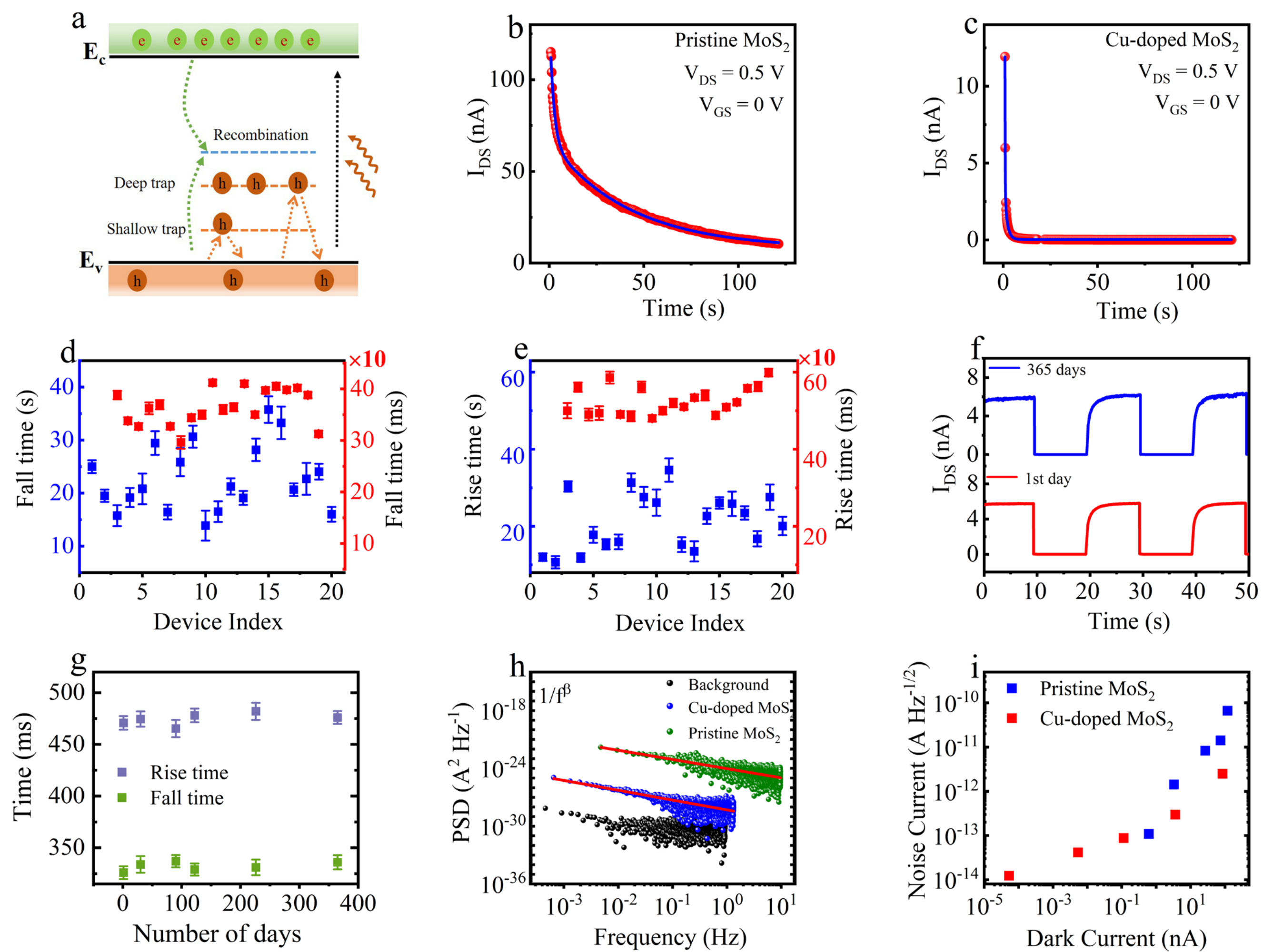

a
E$_c$
E$_v$
Recombination
Deep trap
Shallow trap
b
Pristine MoS$_2$
V$_{DS}$ = 0.5 V
V$_{GS}$ = 0 V
I$_{DS}$ (nA)
Time (s)
c
Cu-doped MoS$_2$
V$_{DS}$ = 0.5 V
V$_{GS}$ = 0 V
I$_{DS}$ (nA)
Time (s)
d
Fall time (s)
Fall time (ms)
×10
Device Index
e
Rise time (s)
Rise time (ms)
×10
Device Index
f
365 days
1st day
I$_{DS}$ (nA)
Time (s)
g
Rise time
Fall time
Time (ms)
Number of days
h
1/f^β
Background
Cu-doped MoS$_2$
Pristine MoS$_2$
PSD (A^2 Hz^{-1})
Frequency (Hz)
i
Pristine MoS$_2$
Cu-doped MoS$_2$
Noise Current (A Hz$^{-1/2}$)
Dark Current (nA)

Table -1 Comparison of pristine MoS_2 n-FETs and Cu-doped MoS_2 p-branch with representative high-performance n-type and p-type FETs.

Ref	Growth / Material / Type	Dielectric	L_{ch} (nm)	V_{DS} (V)	I_{ON} (μA/μm)	SS (mV dec^{-1})	V_{TH} (V)	I_{ON} /I_{OFF}
40	MOCVD MoS_2 (n-FET)	10 nm HfO_2	100	1	336	83	1	> 10^7
70	MOCVD WSe_2 (n-FET)	9 nm Al_2O_3 /3 nm HfO_2/3 nm Al_2O_3	300	1	26	142	1.35	10^7
71	MOCVD MoS_2 (n-FET)	9 nm Al_2O_3 /3 nm HfO_2/3 nm Al_2O_3	300	1	33	79	2.7	> 10^7
This work	Pristine MoS_2 (n-FET)	300 nm SiO_2	4000	0.5	0.18	5600	−8V	~ 10^6
40	MOCVD WSe_2 (p-FET)	10 nm HfO_2	100	1	306	74	− 0.85	10^8
70	MOCVD WSe_2 (p-FET)	9 nm Al_2O_3 /3 nm HfO_2/3 nm Al_2O_3	300	1	16	244	− 0.84	10^7
71	MOCVD WSe_2 (p-FET)	9 nm Al_2O_3 /3 nm HfO_2/3 nm Al_2O_3	300	1	10	450	-2	10^7
20	MOCVD WSe_2 (p-FET)	10 nm HfO_2	100	-1	280	350	− 0.5	10^7
21	CVT $MoSe_2$ (p-FET)	25 nm Al_2O_3	50	1	212	3000	–	10^4
72	MOCVD WSe_2 (p-FET)	25 nm Al_2O_3	20	1	16	770	2	10^5
This work	Cu-doped MoS_2 (p-branch)	300 nm SiO_2	4000	0.5	$2×10^{-5}$	--	~ −20	~ 10^2

ARTICLE IN PRESS

ARTICLE IN PRESS

Table -2 Comparison of photodetector performance of MoS2-based devices.

Ref	Channel	Area	λ (nm)	P_{in} (mw/cm^2)	R (A/W)	D* (jones)	NEP (W Hz$^{-1/2}$)	τ_{rise} / τ_{fall}	V_{DS} /V_{GS} (V)
87	MoS_2	1μm × 5μm	450-625	2	3.6 × 10^7	5.6× 10^{13}	–	10 ms /0.1 ms	6/5
5	MoS_2	2.1μm × 2.6μm	450	–	4.2 × 10^{-4}	–	–	50 ms /50 ms	1/0
13	MoS_2	–	561	0.024	881	–	1.8 × 10^{-15}	4 s/9 s	8/-70
88	MoS_2	–	470	10	17.4	2.48 × 10^{12}	–	8/8.5	0.5/0
This work	Pristine MoS_2	4 μm × 10 μm	470	8	313	2.4×10^{10}	1.6 × 10^{-14}	16 s / 22 s	0.5/0
This work	Cu-doped MoS_2	4 μm × 10 μm	470	8	15.6	3.5×10^{13}	6.4 × 10^{-16}	529 ms / 347 ms	0.5/0

ARTICLE IN PRESS